

## REVERBERATION MEASUREMENTS FOR 17 QUASARS AND THE SIZE-MASS-LUMINOSITY RELATIONS IN ACTIVE GALACTIC NUCLEI

SHAI KASPI,<sup>1,2</sup> PAUL S. SMITH,<sup>3</sup> HAGAI NETZER,<sup>1</sup> DAN MAOZ,<sup>1</sup> BUELL T. JANNUZI,<sup>3</sup> AND URIEL GIVEON<sup>1</sup>

Accepted Version (November 22, 1999)

### ABSTRACT

Correlated variations in the line and continuum emission from active galactic nuclei (AGN) can be used to determine the size and geometry of the broad emission line regions (BLRs). We have spectrophotometrically monitored a well-defined sample of 28 Palomar-Green quasars in order to obtain measurements of their BLRs and to investigate the relationships between quasar luminosity, central black hole mass, and BLR size in AGN. Spectrophotometry was obtained every 1–4 months for 7.5 years, yielding 20–70 observing epochs per object. Both the continuum and emission line fluxes of all of the quasars were observed to change during the duration of the observing program. Seventeen of the 28 objects were observed with adequate sampling ( $\gtrsim 20$  independent observing epochs) to search for correlated variations between the Balmer emission lines and the continuum flux. For each of these 17 objects, a significant correlation was observed, with the Balmer line variations lagging those of the continuum by  $\sim 100$  days (rest frame). Our work increases the available luminosity range for studying the size–mass–luminosity relations in AGN by two orders of magnitude and doubles the number of objects suitable for such studies. Combining our results with comparable published data available for Seyfert 1 galaxies, we find the BLR size scales with the rest-frame 5100 Å luminosity as  $L^{0.70 \pm 0.03}$ . This determination of the scaling of the size of the BLR as a function of luminosity is significantly different from those previously published, and suggests that the effective ionization parameter in AGN may be a decreasing function of luminosity. We are also able to constrain, subject to our assumption that gravity dominates the motions of the BLR gas, the scaling relationship between the mass of the central black holes and the luminosity in AGN. We find that the central mass scales with 5100 Å luminosity as  $M \propto L^{0.5 \pm 0.1}$ . This is inconsistent with all AGN having optical luminosity that is a constant fraction of the Eddington luminosity.

*Subject headings:* galaxies: active — quasars: emission lines — quasars: general

### 1. INTRODUCTION

Reverberation mapping, observing the degree and nature of the correlation between continuum and emission line flux variations, is one of the major tools for studying the distribution and kinematics of the gas in the broad line region (BLR) of active galactic nuclei (AGN; see reviews by Peterson 1993 and by Netzer & Peterson 1997). About 17 low luminosity AGN (Seyfert 1 galaxies) have been successfully monitored and produce statistically meaningful results (see Wandel, Peterson, & Malkan 1999, and references therein). Best studied among these is the Seyfert 1 galaxy, NGC 5548, which was monitored from the ground for over eight years, and from space for several long periods (Peterson et al. 1999, and references therein). Several other Seyfert 1s were observed for periods of order 1 year or less, and nine Seyfert 1s were studied over a period of eight years (Peterson et al. 1998a). The measured time lags between the emission lines and the continuum light curves in these objects can be interpreted in terms of the delayed response of a spatially-extended BLR to a variable, compact source of ionizing radiation. While the observations do not uniquely determine the geometry of the BLR, they give its typical size which, for Seyfert 1 galaxies, is of the order of light-days to several light-weeks ( $\sim 10^{16}$ – $10^{17}$  cm). Recent studies have shown that the time lags determined in NGC 5548 for different observing seasons correlate with the seasonal luminosity of the object (Pe-

terson et al. 1999), and have presented evidence for Keplerian motions of the BLR gas (Peterson & Wandel 1999).

While Seyfert 1 galaxies have been studied successfully using reverberation mapping, few similar studies of the more luminous AGN – the quasars – have been presented. Those that have been published have been limited in their success at determining the properties of the quasar BLRs. Past attempts to monitor quasars spectrophotometrically have generally suffered from temporal sampling and/or flux calibrations that are not sufficient for the determination of the BLR size. Zheng and collaborators (Zheng & Burbidge 1986, Zheng et al. 1987, and Zheng 1988) reported results of a monitoring program executed on 30 quasars for several years, with a sampling interval of about one year. They found the emission-line flux to change in response to the continuum changes, but because of the limited time resolution, only an upper limit of about one light-year for the BLR size could be deduced. Several other groups (Pérez, Penston, & Moles 1989, Korista 1991, Jackson et al. 1992, and Erkens et al. 1995) observed samples of quasars for approximately one year sampled with monthly observations. Each of these groups reported line variations on time scales of a few months, but because of the short duration of these programs the data were insufficient for more specific conclusions. Wisotzki et al. (1998) monitored the gravitationally lensed quasar HE 1104–1805 for five years. Although the quasar continuum varied considerably, the emission line fluxes

<sup>1</sup>School of Physics and Astronomy and the Wise Observatory, The Raymond and Beverly Sackler Faculty of Exact Sciences, Tel-Aviv University, Tel-Aviv 69978, Israel.

<sup>2</sup>Current address: Department of Astronomy & Astrophysics, The Pennsylvania State University, University Park, PA 16802. E-mail: shai@astro.psu.edu.

<sup>3</sup>National Optical Astronomy Observatories, P.O. Box 26732, Tucson, AZ 85719.

appeared to remain constant. Researchers have also attempted to use spectra obtained with the *International Ultraviolet Explorer (IUE)* and reverberation mapping techniques to study AGN. In particular, several studies (Gondhalekar et al. 1986, Gondhalekar 1990, Sitko 1990, O'Brien & Gondhalekar 1991, and Koratkar et al. 1998) deduced BLR sizes of 0.01–2 light-years for AGN. However, these results are controversial due to insufficient sampling and/or uncertainty regarding the absolute flux calibrations of the IUE observations (e.g., Bohlin & Grillmair 1988a, 1988b). Even the quasar best studied by IUE, 3C 273, has yielded disputed results when different researchers have analyzed similar IUE data sets. Both O'Brien & Harries (1991) and Koratkar & Gaskell (1991a) found a measurable and similar lag between continuum and BLR variations, while Ulrich, Courvoisier, & Wamsteker (1993) argue that the line variations reported in the earlier studies were only marginally significant. Thus, even in the best-studied case, past results have proven controversial.

To obtain more definite results on the BLR size in quasars, we began monitoring a well-defined sub-sample of 28 quasars from the Palomar-Green (PG) sample (Schmidt & Green 1983) in 1991 March at the Wise and Steward Observatories. Results from the first 1.5 years were presented in Maoz et al. (1994; Paper I) where it was shown that most quasars underwent continuum variations (at 4800 Å rest wavelength) with amplitudes of 10% – 70%. Balmer-line variability, correlated with the continuum variations, was detected in several objects. The preliminary data showed that the typical response time of the emission lines is  $\lesssim 6$  months. Reverberation mapping of such objects therefore requires several years, with sampling intervals of less than a few months. Further results, based on four years of monitoring two quasars from our sample, PG 0804+761 and PG 0953+414, were presented in Kaspi et al. (1996a; Paper II). The measured time lags between the Balmer lines and the continuum variations of the quasars suggested that the BLR size grows roughly as the square root of the luminosity of the nucleus. Wandel et al. (1999) confirmed this result using a larger sample of AGN.

During the period of our spectrophotometric project we also monitored several quasar samples photometrically in the *B* and *R* bands. The broad-band results for radio- and optically-selected samples were presented in Netzer et al. (1996) and Giveon et al. (1999; hereafter Paper III), respectively. The optical sample in Paper III consists of 42 PG quasars, including all 28 objects discussed in the present paper.

The present paper presents final results from 7.5 years of spectroscopic monitoring of our sample. In § 2 we describe the sample, observations, data reduction, and present the light curves. In § 3 we perform a time series analysis to determine the response time of the emission-line flux to continuum variations. We estimate the BLR size, continuum luminosity, and central mass for each quasar in § 4, and in § 5 we discuss the relations among these properties.

## 2. SAMPLE, OBSERVATIONS, AND REDUCTION

The sample, observing technique, and the reduction procedure, are described in detail in Papers I, II, & III. For the sake of completeness, we briefly repeat them here, with emphasis on the few procedures which, in the final reduction, were modified with respect to previous descriptions. The sample consists

of 28 PG quasars. Objects with a northern declination,  $B < 16$  mag (based on the magnitudes given in Schmidt & Green 1983), redshift  $z < 0.4$ , and a bright comparison star within 3.5' of the quasar, were selected. Table 1 presents detailed information about the sample. Throughout this paper we will use only the first four digits in the PG object name to identify individual objects.

The observations were carried out using the Steward Observatory (SO) 2.3m telescope and the Wise Observatory (WO) 1m telescope. Throughout the years different detectors were used. At SO we used the Boller & Chivens spectrograph with a 300 l/mm grating, a 4.5"-wide slit and a TI CCD. In 1992 September this CCD was replaced with a 1200×800 Loral CCD. At WO the Faint Object Spectroscopic Camera (FOSC; Kaspi et al. 1995) was used with a 15"-wide slit and a front-illuminated 1024×1024 TI CCD as a detector. In 1994 February the slit was replaced by a 10"-wide slit and the detector used was a 1024×1024 back-illuminated Tektronix CCD. The typical wavelength coverage, at both observatories, was  $\sim 4000$ –8000 Å, with a dispersion of  $\sim 3.8$  Å/pixel, and a spectral resolution of  $\sim 10$  Å.

Spectrophotometric calibration for every quasar was accomplished by rotating the spectrograph slit to the appropriate position angle so that a nearby comparison star (columns [11] & [12] in Table 1) was observed simultaneously with the object. A wide slit was used to minimize the effects of atmospheric dispersion at the non-parallactic position angle. This technique provides excellent calibration even during poor weather conditions, and accuracies of order 1% – 2% can easily be achieved.

Observations typically consisted of two consecutive exposures of the quasar/star pair. Total exposure times were usually 40 minutes at the SO 2.3m telescope and 2 hours at the WO 1m telescope. The spectroscopic data were reduced using standard IRAF<sup>4</sup> routines. The consecutive quasar/star flux ratios were compared to test for systematic errors in the observations and to clean cosmic rays. The ratio usually reproduced to 0.5–2.5% at all wavelengths and observations with ratios larger than 5% were discarded. We verified that none of our comparison stars are variable to within  $\sim 2\%$  by means of differential photometry with other stars in each field (Paper III). Spectra were calibrated to an absolute flux scale using observations of spectrophotometric standard stars on one or more epochs. The absolute flux calibration has an uncertainty of  $\sim 10\%$ , which is not shown in the error bars in our light curves. The error bars reflect only the measurement and differential uncertainties, which are of order 1%–2%.

For each quasar we used all the spectra to produce an average spectrum and a root-mean-square (rms) spectrum, defined as:

$$\sigma(\lambda) = \left\{ \frac{1}{(N-1)} \sum_{i=1}^N [f_i(\lambda) - \bar{f}(\lambda)]^2 \right\}^{1/2}, \quad (1)$$

where the sum is taken over the  $N$  spectra, and  $\bar{f}(\lambda)$  is the average spectrum (Peterson et al. 1998a). The mean spectra of all the quasars in our sample are shown in Fig. 1. An example of a typical rms spectrum and comparison with the mean spectrum is shown in Fig. 2 for PG 0844. We used the average and rms spectra to choose line-free spectral bands suitable for setting the continuum underlying the emission lines, and the wavelength limits for integrating the line fluxes. The spec-

<sup>4</sup>IRAF (Image Reduction and Analysis Facility) is distributed by the National Optical Astronomy Observatories, which are operated by AURA, Inc., under cooperative agreement with the National Science Foundation.

TABLE 1  
SAMPLE PROPERTIES

Object (1)	RA (1950.0) (2)	Dec (3)	z (4)	$m_B$ (5)	$M_B$ (6)	$A_B$ (7)	$N_{phot}$ (8)	$N_{spec}$ (9)	$f_{\lambda}(5100\text{\AA})$ (10)	$R_{comp}$ (11)	$\text{PA}_{comp}$ (12)
PG 0026+129	00 26 38.1	12 59 30	0.142	15.3	-23.7	0.13	38	56	$26.9 \pm 4.0$	95	42.0
PG 0052+251	00 52 11.1	25 09 24	0.155	14.7	-24.1	0.12	41	56	$20.7 \pm 3.7$	92	153.4
PG 0804+761	08 04 35.4	76 11 32	0.100	14.5	-23.7	0.11	38	70	$54.8 \pm 10.0$	182 <sup>a</sup>	315.6 <sup>a</sup>
PG 0844+349	08 44 33.9	34 56 09	0.064	15.1	-22.1	0.08	31	49	$37.1 \pm 3.8$	124	36.8
PG 0953+414	09 53 48.3	41 29 58	0.239	15.4	-24.5	0.00	38	36	$15.6 \pm 2.1$	104	31.7
PG 1048+342	10 48 56.1	34 15 23	0.167	17.7	-21.9	0.00	30	1	$5.51 \pm 0.28$	186	94.7
PG 1100+772	11 00 27.4	77 15 09	0.313	15.9	-24.7	0.06	46	9	$7.72 \pm 0.23$	68	84.1
PG 1202+281	12 02 08.9	28 10 54	0.165	16.2	-23.0	0.03	37	9	$7.2 \pm 2.0$	73	219.8
PG 1211+143	12 11 44.8	14 19 53	0.085	14.4	-23.4	0.13	52	38	$56.6 \pm 9.2$	162	352.2
PG 1226+023	12 26 33.4	02 19 42	0.158	12.8	-26.3	0.00	26	39	$213 \pm 26$	171	171.2
PG 1229+204	12 29 33.1	20 26 03	0.064	15.5	-21.7	0.00	32	33	$21.5 \pm 2.3$	75	291.5
PG 1307+085	13 07 16.2	08 35 47	0.155	15.6	-23.5	0.02	35	23	$17.9 \pm 1.8$	138	186.5
PG 1309+355	13 09 58.5	35 31 15	0.184	15.5	-24.0	0.00	30	9	$23.6 \pm 1.4$	167	74.2
PG 1322+659	13 22 08.5	65 57 25	0.168	16.0	-23.3	0.05	27	8	$11.60 \pm 0.74$	104	277.5
PG 1351+640	13 51 46.3	64 00 28	0.087	14.7	-23.2	0.03	40	30	$51.4 \pm 5.1$	109	196.5
PG 1354+213	13 54 11.5	21 18 30	0.300	17.3	-23.2	0.04	25	3	$11.14 \pm 0.25$	125	133.4
PG 1402+261	14 02 59.2	26 09 51	0.164	15.6	-23.6	0.00	27	6	$18.73 \pm 0.87$	171	334.8
PG 1404+226	14 04 02.5	22 38 03	0.098	16.5	-21.8	0.01	27	8	$11.40 \pm 0.91$	77	223.0
PG 1411+442	14 11 50.1	44 14 12	0.089	15.0	-22.9	0.00	34	24	$37.1 \pm 3.2$	128	347.0
PG 1415+451	14 15 04.3	45 09 57	0.114	16.3	-22.3	0.00	29	3	$15.2 \pm 1.8$	189	95.2
PG 1426+015	14 26 33.8	01 30 27	0.086	15.7	-22.2	0.12	33	20	$46.2 \pm 7.1$	106	341.4
PG 1444+407	14 44 50.2	40 47 37	0.267	17.4	-23.0	0.00	27	5	$9.98 \pm 0.39$	158	155.4
PG 1512+370	15 12 46.9	37 01 56	0.371	16.4	-24.5	0.05	35	10	$4.82 \pm 0.76$	63	284.9
PG 1613+658	16 13 36.3	65 50 38	0.129	14.9	-23.8	0.04	42	48	$34.9 \pm 4.3$	101	164.2
PG 1617+175	16 17 56.2	17 31 34	0.114	15.5	-22.8	0.15	39	35	$14.4 \pm 2.5$	147	253.0
PG 1700+518	17 00 13.4	51 53 37	0.292	15.4	-25.2	0.02	41	39	$22.0 \pm 1.5$	104	183.5
PG 1704+608	17 04 03.5	60 48 31	0.371	15.6	-25.5	0.00	39	25	$16.6 \pm 2.4$	114	188.2
PG 2130+099	21 30 01.2	09 55 01	0.061	14.7	-22.4	0.17	47	64	$48.4 \pm 4.5$	86	68.2

## Notes.—

(1) Object name, as it appears in Schmidt & Green (1983).  
 (2)–(3) Right Ascension and Declination (1950).  
 (4) Redshift.  
 (5)–(6) Median (over all epochs) apparent and absolute  $B$  magnitudes from Paper III.  
 (7) Galactic  $B$ -band extinction,  $A_B$ , from NED. See § 4.2.  
 (8)–(9) Number of photometric and spectrophotometric observing epochs.  
 (10) Average flux density and its rms at rest wavelength  $\sim 5100 \text{\AA}$  in units of  $10^{-16} \text{ ergs s}^{-1} \text{ cm}^{-2} \text{\AA}^{-1}$  (see Table 2 column (7) for exact wavelength intervals).  
 (11)–(12) The angular separation in arcseconds and position angle in degrees of the comparison star (see § 2).

<sup>a</sup>Comparison star at SO:  $R_{comp} = 119''$ ,  $\text{PA}_{comp} = 64.3$  degrees.

TABLE 2  
INTEGRATION LIMITS FOR CONTINUUM BANDS AND EMISSION LINES

Object (1)	Continuum (2)	$H\gamma$ (3)	Continuum (4)	Continuum (5)	$H\beta$ (6)	Continuum (7)	Continuum (8)	$H\alpha$ (9)	Continuum (10)
PG 0026	4790–4830	4920–5045	5070–5100	<b>5408–5468</b>	5508–5654	5818–5868	6998–7138	7304–7728	7730–7790
PG 0052	<b>4864–4914</b>	4926–5118	5418–5488	5418–5488	5518–5698	5908–5978	7028–7108	7398–7724	7725–7800
PG 0804	4680–4705	4710–4850	4880–4905	<b>5224–5264</b>	5266–5474	5598–5630	6746–6814	6940–7412	7472–7520
PG 0953	<b>5238–5278</b>	5284–5450	5472–5506	5846–5892	5906–6086	6288–6320	...	...	...
PG 1211	4525–4560	4625–4755	4780–4810	<b>5120–5160</b>	5180–5340	5490–5530	6670–6720	6900–7310	7480–7540
PG 1226	4925–4945	4946–5130	<b>5135–5165</b>	5494–5522	5530–5756	5888–5928	7034–7085	7250–7788	7789–7808
PG 1229	4500–4560	4560–4690	4694–4758	5052–5088	5094–5244	<b>5412–5456</b>	6562–6654	6838–7148	7244–7320
PG 1307	4870–4915	4938–5088	5104–5154	<b>5458–5488</b>	5508–5698	5864–5914	7050–7100	7400–7740	7750–7800
PG 1351	4585–4645	4646–4781	4815–4850	<b>5048–5128</b>	5196–5352	5545–5605	6638–6770	6898–7322	7362–7432
PG 1411	4570–4600	4650–4790	4805–4835	<b>5155–5185</b>	5201–5382	5520–5555	6700–6760	6870–7360	7490–7560
PG 1426	4565–4605	4605–4775	4730–4796	<b>5105–5145</b>	5170–5360	5515–5555	6680–6730	6930–7270	7490–7550
PG 1613	...	...	...	<b>5300–5350</b>	5360–5566	5740–5790	7000–7050	7013–7742	7743–7803
PG 1617	4650–4700	4745–4950	4930–4960	<b>5250–5295</b>	5310–5550	5672–5722	6898–6968	7118–7498	7540–7580
PG 1700	...	...	...	<b>6030–6080</b>	6120–6410	6520–6570	7760–8015	8245–8689	8690–8730
PG 1704	5800–5865	5900–6025	<b>6040–6100</b>	6460–6520	6575–6735	7020–7100	...	...	...
PG 2130	4460–4490	4533–4710	4710–4735	<b>5048–5084</b>	5094–5240	5394–5440	6498–6598	6798–7118	7246–7318

Note.—Wavelengths in units of  $\text{\AA}$  at the observer's frame. The bold-font ranges are the continuum bands shown in Fig. 3.

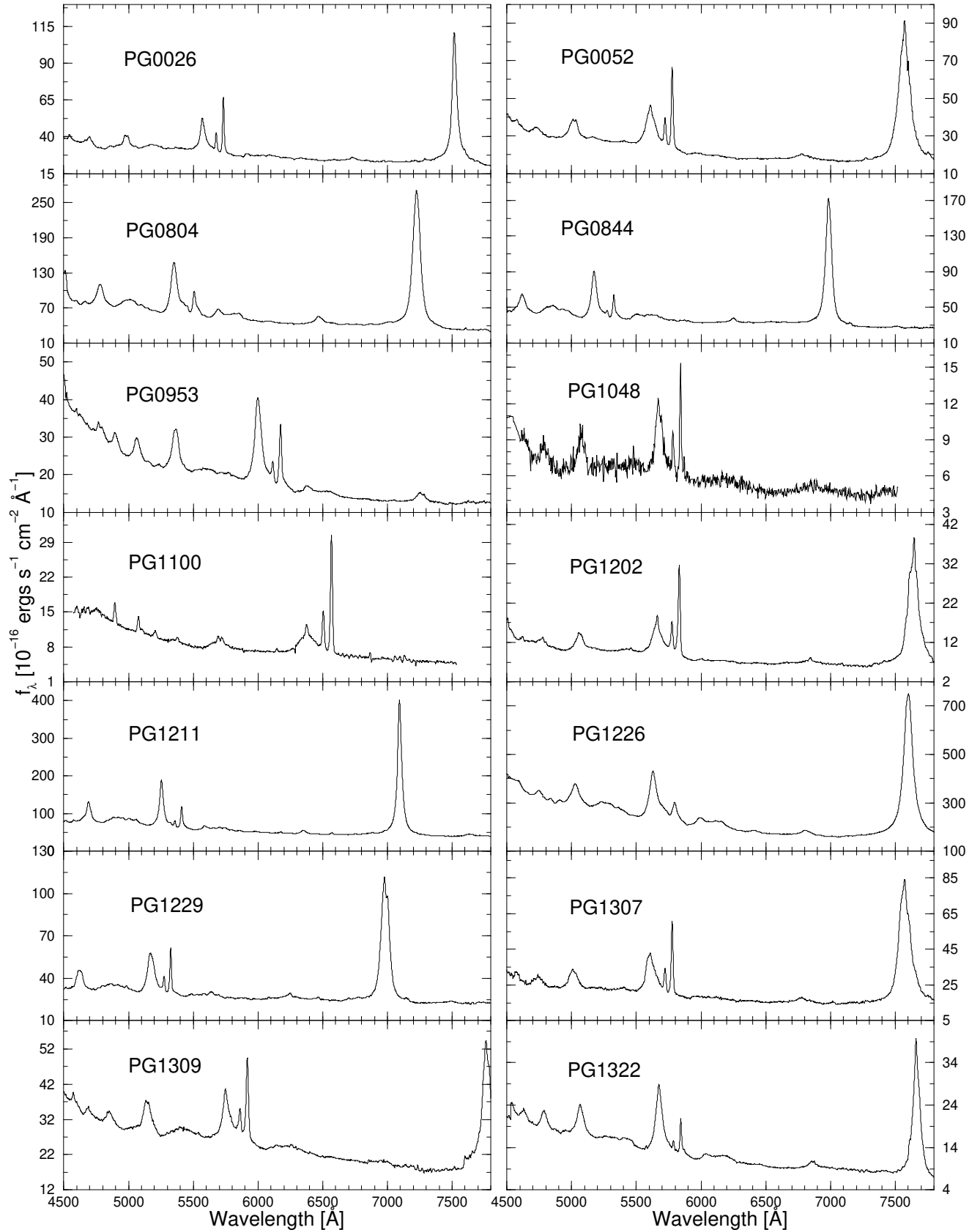


FIG. 1.— Mean spectra of PG quasars in the observed frame.

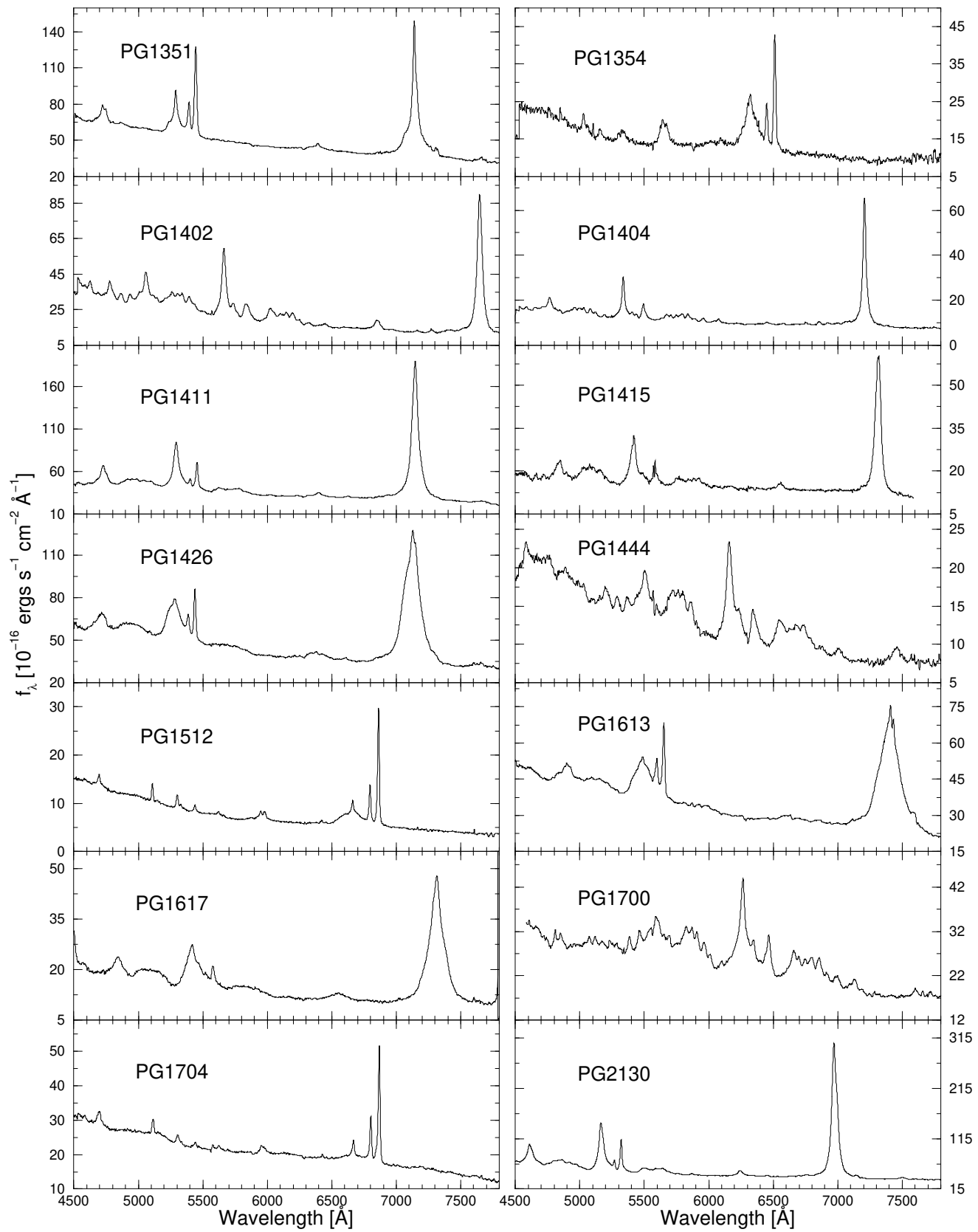


FIG. 1.—Continued

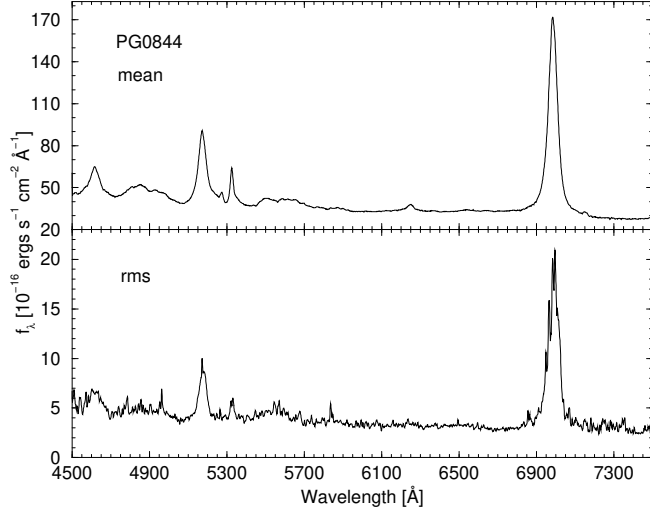


FIG. 2.— PG 0844 mean spectrum (*top*) and rms spectrum (*bottom*).

tral intervals for the Balmer lines and the continuum bands on both sides of each line are given in Table 2. The line and continuum fluxes were measured algorithmically for all epochs by calculating the mean flux in the continuum bands, and summing the flux above a straight line in  $f_\lambda$  that connects the continuum bands straddling the emission line. This process measures the total emission in each line, i.e., the flux of the broad component of the line together with its narrow component. The uncertainty in the line flux was estimated by propagating the uncertainty in the setting of the continuum levels, determined from the standard deviation of the mean in the continuum bands. To this we added in quadrature our estimate for the uncertainty in the differential spectrophotometry.

For the purpose of time series analysis, we generally chose a region just blue of  $H\beta$  for the continuum band. In several cases where the blue side of  $H\beta$  has an inferior light curve (due to, e.g., atmospheric absorption bands and/or superposed emission line blends) we chose continuum bands around  $H\gamma$ . Table 2 lists in bold font the continuum band chosen for each object. Both the continuum bands and the emission lines can be affected by the contribution of variable Fe II lines. However, correcting for this effect is beyond the scope of the present study. Similarly, our Balmer line measurements might be contaminated by narrow forbidden emission-lines. Though we measure  $H\beta$  without the  $[\text{O III}]\lambda\lambda 4995, 5007$  lines (since there is a clear separation between them) we cannot do so for the  $[\text{N II}]\lambda\lambda 6548, 6583$  lines blended with the  $H\alpha$  line. However, we note that contamination from narrow lines should not affect our time series analysis since this analysis relies on the variable parts of the lines, and the narrow lines have never been observed to vary in AGN over relevant time scales (e.g., Kaspi et al. 1996b).

The AGN continuum dominates the emission-line flux and host galaxy starlight contribution to the broad-band photometry. To improve the sampling of the continuum light curves, we therefore merged the photometric  $B$  band light curves of Paper III into the spectrophotometric continuum light curves (see Paper I). The photometric campaign lasted 7 years and we extended the observations of the present 28 objects for six more months to better overlap with the spectrophotometric campaign. Those last photometric observations were reduced and added to the light curves as explained in Paper III.

The photometric and spectrophotometric light curves of each object were intercalibrated by comparing all pairs of spectrophotometric and photometric observations separated in time by less than a few days (typically  $\sim 5$  days, and in some cases up to  $\sim 10$  days). This produced 10 to 15 pairs of points per object. A linear least-squares fit between the spectrophotometric continuum fluxes and the photometric fluxes (the magnitudes of Paper III translated to fluxes) was used to merge the two light curves.

For each object, the total number of photometric and spectrophotometric observations is given in Table 1, columns (8) & (9) (the sum of the two columns gives the total number of points in the continuum light curve). Note that for particular emission-lines in a few objects, some data points are missing because of cosmic-rays contaminations, insufficient wavelength coverage, or low S/N. Light curves for the 17 objects that have more than 20 spectrophotometric data points are presented in Fig. 3 with the data listed in Table 3 and Table 4<sup>5</sup>. Each of the remaining 11 objects in our sample have less than 10 spectrophotometric observations over the 7.5 year period. Such rare sampling is insufficient to determine the line-to-continuum lag and these objects will not be discussed further in this paper.

### 3. TIME SERIES ANALYSIS

The continuum variability properties of our quasar sample are extensively discussed in Paper III. All 17 objects underwent optical continuum variability (at 5100 Å rest wavelength) of 25%–150%, measured relative to the minimum flux. In order to compare the line variability to the continuum variability in each quasar, we define an intrinsic normalized variability measure,  $\sigma_N = 100\sqrt{\sigma^2 - \delta^2}/\bar{f}$ , where  $\bar{f}$  and  $\sigma$  are the average and the rms of the flux in a given light curve, respectively, and  $\delta$  is the mean uncertainty of all data points in that light curve. This measure is less sensitive to noise and outliers than the minimum-to-maximum flux ratio. The two cases where  $\sigma^2 - \delta^2$  is slightly negative ( $H\gamma$  in PG 1426 and PG 1617) are consistent with no variability. Table 5 summarizes  $\sigma_N$  for the 5100 Å rest frame continua band and all of the available emission-line light curves. In general we find that all of the Balmer emission lines in a specific object have about the same level of variability. In

<sup>5</sup>A machine-readable version of these data is available upon request from the authors, or at URL: <http://wise-obs.tau.ac.il/~shai/PG/>

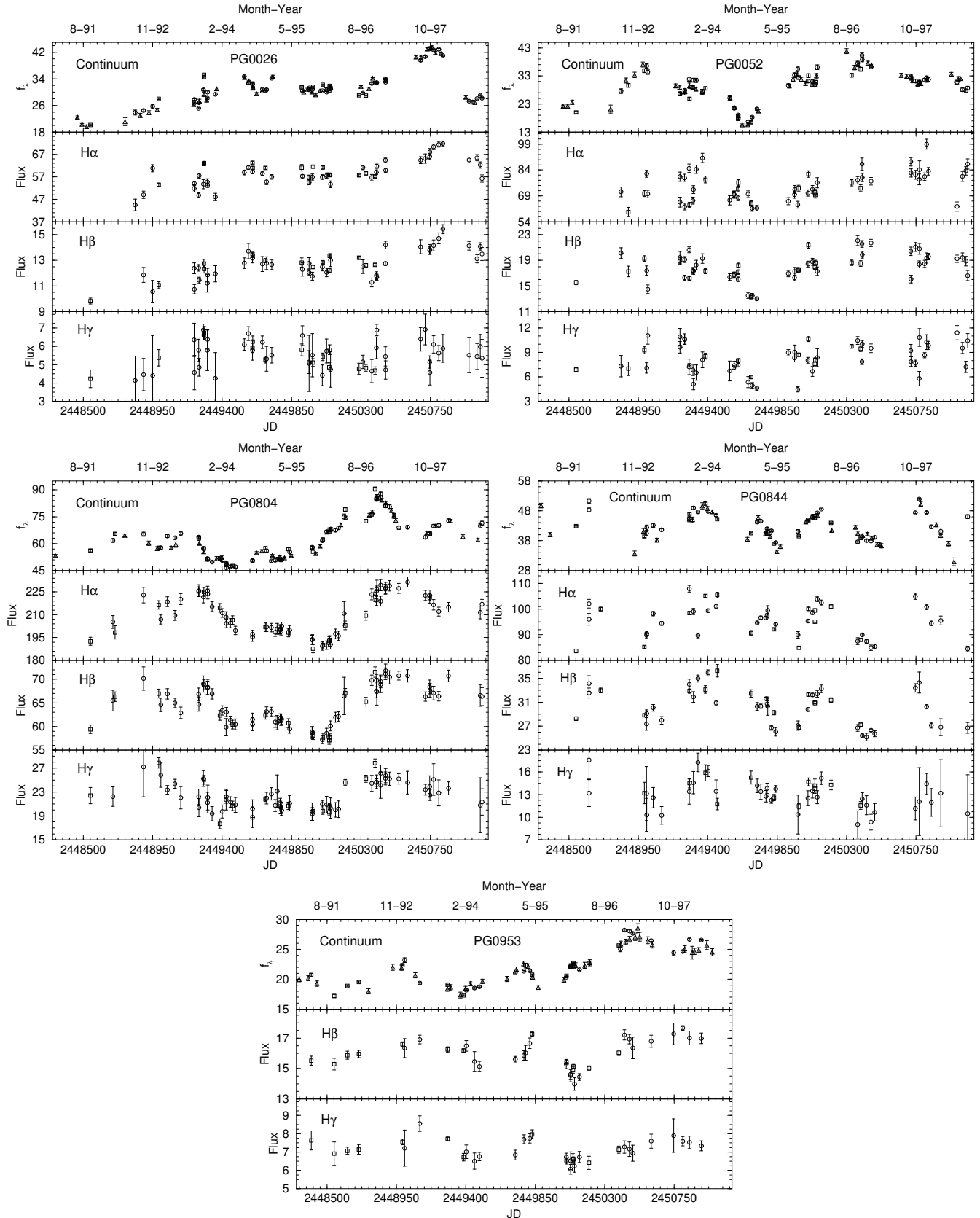


FIG. 3.— Light curves for 17 PG quasars. Circles are spectrophotometric data from WO, squares are spectrophotometric data from SO, triangles are photometric data from WO. Continuum flux densities,  $f_{\lambda}$ , are determined from the wavelength bands listed in bold-font in Table 2, and are given in units of  $10^{-16} \text{ ergs s}^{-1} \text{ cm}^{-2} \text{ \AA}^{-1}$ . Emission-line fluxes are displayed in units of  $10^{-14} \text{ ergs s}^{-1} \text{ cm}^{-2}$ . Horizontal axis given in Julian Day (bottom) and UT date (top).

## REVERBERATION AND SIZE-MASS-LUMINOSITY

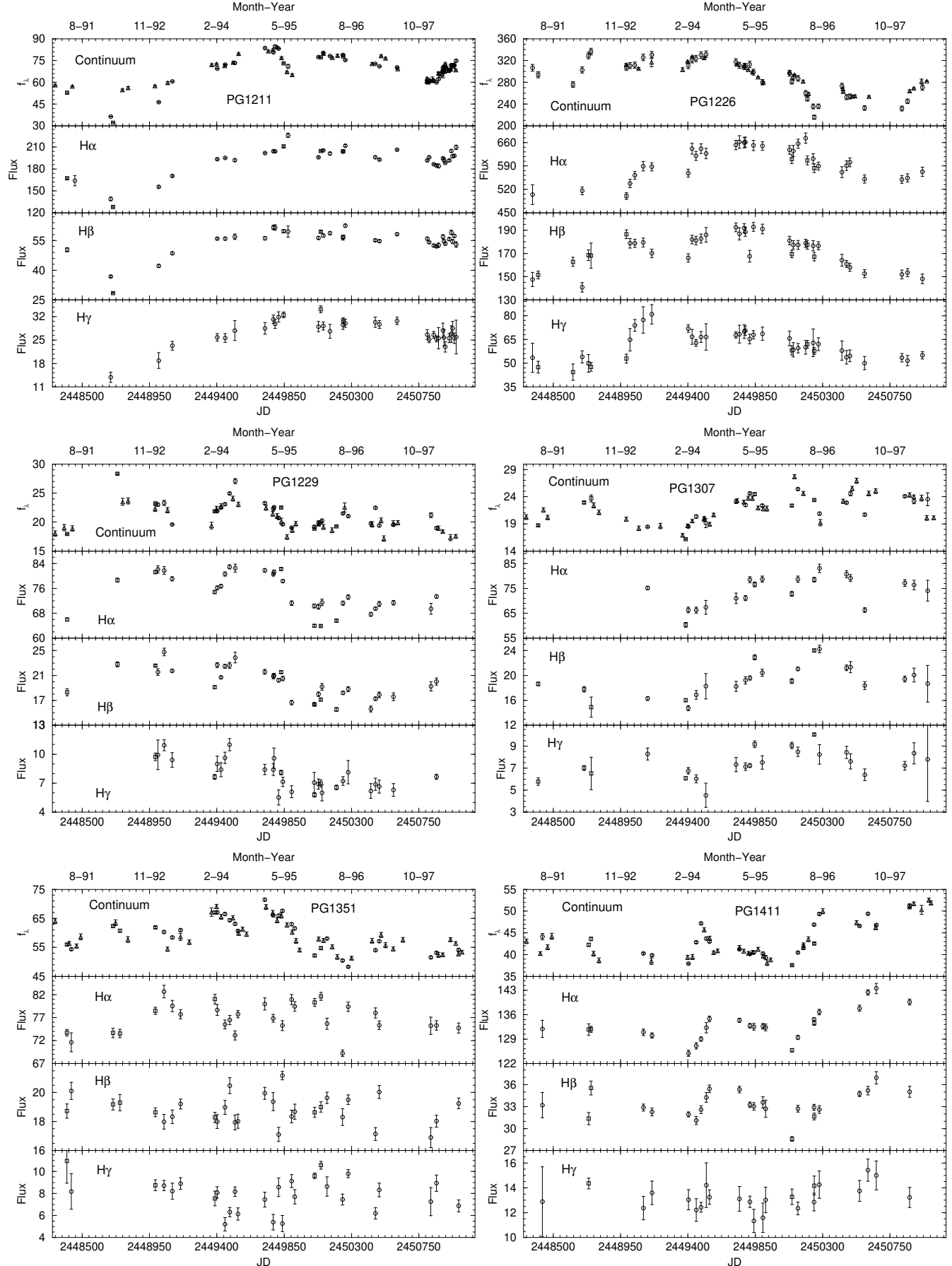


FIG. 3.—Continued

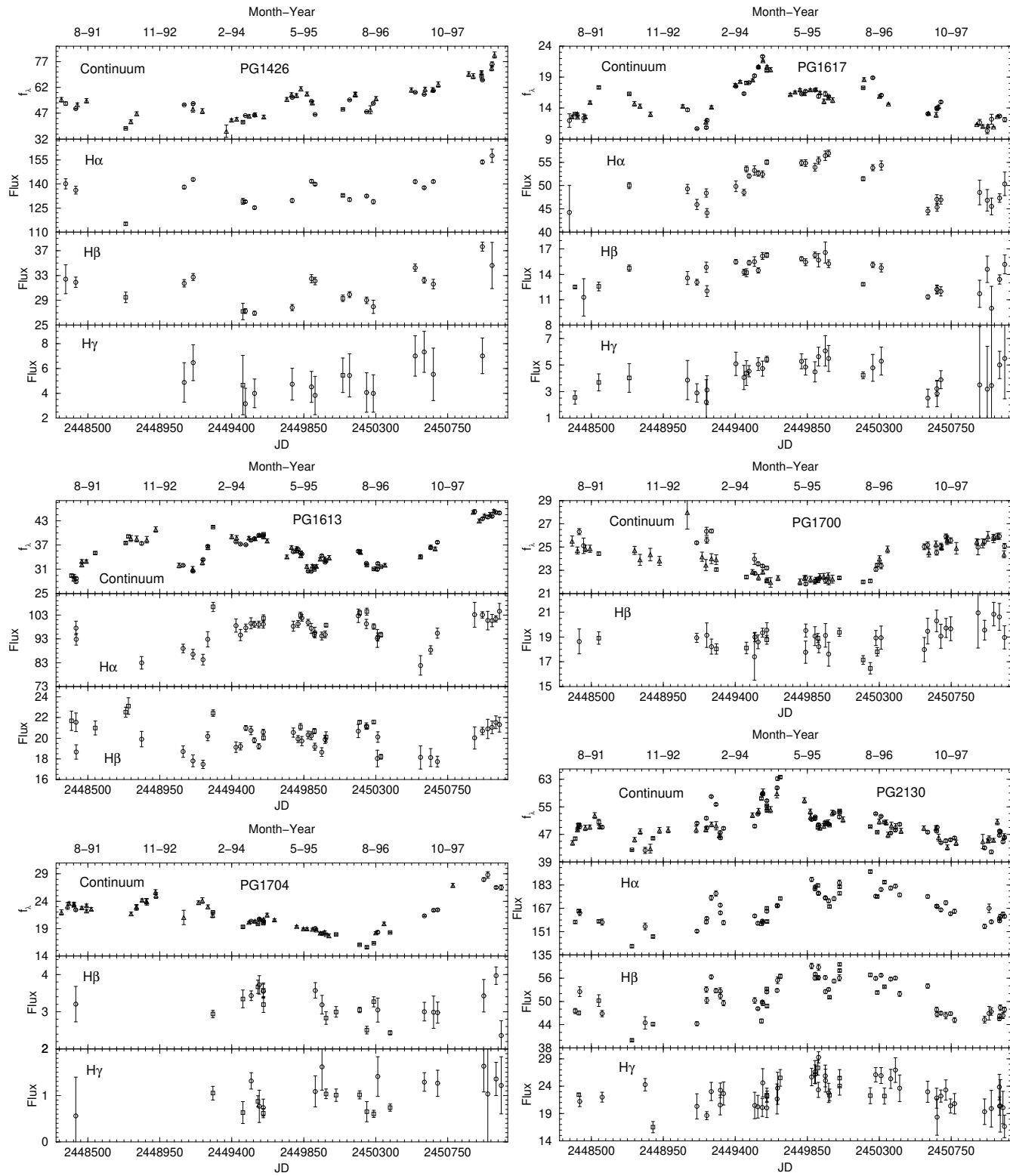


FIG. 3.—Continued

all objects, the variability of the emission lines is smaller than the continuum variability. In the few cases where those trends do not hold, it appears that they may be masked by noise (e.g., most cases in which the emission line varies with a larger amplitude than the continuum involve  $H\gamma$ , which has lower S/N than  $H\alpha$  and  $H\beta$ ).

The main goal of this project is to determine the time lag between the continuum and the Balmer-line flux variations in high-luminosity AGN. To quantify this lag, we use two methods for correlating the line and continuum light curves. The first method is the interpolated cross-correlation function (ICCF) of Gaskell & Sparke (1986) and Gaskell & Peterson (1987), as implemented by White & Peterson (1994; see also a review by Gaskell 1994). The second method is the  $z$ -transformed discrete correlation function (ZDCF) of Alexander (1997) which is an improvement on the discrete correlation function (DCF; Edelson & Krolik 1988). The ZDCF applies Fisher's  $z$  transformation to the correlation coefficients, and uses equal population bins rather than the equal time bins used in the DCF. The two independent methods are in excellent agreement for these data and we will use only the ICCF results in the following analyses.

The uncertainties in the cross correlation lag determination can be estimated using the model-independent FR/RSS Monte Carlo method described by Peterson et al. (1998b). In this method, each Monte Carlo simulation is composed of two parts: The first is a "random subset selection" (RSS) procedure which consists of randomly drawing, with replacement, from a light curve of  $N$  points a new sample of  $N$  points. After the  $N$  points are selected, the redundant selections are removed from the sample such that the temporal order of the remaining points is preserved. This procedure reduces the number of points in each light curve by a factor of  $\sim 1/e$  and accounts for the effect that individual data points have on the cross-correlation. The second part is "flux randomization" (FR) in which the observed fluxes are altered by random Gaussian deviates scaled to the uncertainty ascribed to each point. This procedure simulates the effect of measurement uncertainties. Peterson et al. (1998b) demonstrate that under a wide variety of realistic conditions, the combined FR/RSS procedure yields conservative uncertainties compared to the true situation.

All emission-line light curves presented in Fig. 3 were cross correlated with their corresponding continuum light curves. The results of the cross-correlation analysis are presented in Table 6. The object name is given in Column (1) and the specific Balmer line is listed in column (2). For the ICCF we list the centroid time-lag,  $\tau_{cent}$ , (computed from all points within 80% of the peak value,  $r_{max}$ <sup>6</sup>) in column (3). We define the ICCF peak as the point of maximum correlation and list the peak position,  $\tau_{peak}$ , in column (4), and the peak value,  $r_{max}$ , in column (5). In column (6) we list the total number of points in the emission-line light curve (the total number of points in the continuum light curve is given in Table 1 columns [8] & [9]). The uncertainties given for  $\tau_{cent}$  and  $\tau_{peak}$  were computed with the FR/RSS method using  $\sim 10,000$  Monte Carlo realizations which were used to build up a cross-correlation peak distribution (CCPD; Maoz & Netzer 1989). The range of uncertainties contains 68% of the Monte Carlo realizations in the CCPD and thus would correspond to  $1\sigma$  uncertainties for a normal distribution. In addition to the cross-correlation results, we also list in Table 6 velocity measurements and the average of the observed flux for each line. Column (7) lists the mean full-width at half

maximum (FWHM) of the emission-line, column (8) lists the line FWHM measured from the rms spectrum (see § 4.3 below), and column (9) lists the average of the observed line flux and its rms (calculated from the light curves of Table 4).

Fig. 4 presents the cross-correlation functions (CCFs) for the 40 out of 46 emission-line/continua pairs having peak correlation coefficients above 0.4. All 40 CCFs indicate a positive time lag of the Balmer lines with respect to the optical continuum. The time lags are of order a few weeks to a few months, and the CCF peaks are highly significant for most lines. In a few cases,  $\tau_{cent}$  and  $\tau_{peak}$  are consistent with a zero time lag and we attribute this to the fact that these emission-line light curves are noisy, and to the conservative error estimate of the FR/RSS method. Choosing our best lag determination (see below), i.e., avoiding noisy results obtained from weak lines (generally  $H\gamma$ ), we conclude that a time lag has been detected in one or more of the Balmer lines for all 17 quasars.

When comparing the  $H\beta$  time-lags for PG 0804 and PG 0953 obtained in Paper II to the ones deduced here, we find an increase of about 65% for both objects, although the results are consistent at the  $2\sigma$  level. The luminosities of both objects also increased during the second half of the monitoring period. Changes in the time lag between different observing seasons is seen in lower-luminosity AGN (e.g., NGC 4151 and NGC 5548) and is thought to be a real effect, rather than a result of measurement error. For instance, the BLR may become larger when the object becomes brighter.

#### 4. SIZE, LUMINOSITY, AND MASS DETERMINATION

Converting the observable Balmer emission-line time lags, line widths, and continuum fluxes into interesting physical parameters, namely, BLR sizes, and AGN central masses and luminosities, is not straightforward. We therefore discuss each in some detail below. We analyze our data together with data for other AGN. Wandel et al. (1999) have uniformly analyzed the reverberation mapping data of 17 Seyfert 1s, and deduced time lags using the same techniques described in the previous section. Combining their results with the present ones, we obtain, for the first time, reliable Size–Mass–Luminosity relations for 34 AGN spanning over 4 orders of magnitudes in continuum luminosity. Our analysis is similar to that of Wandel et al. (1999), and the few significant differences are noted below.

We apply below linear regression analysis to the data. Unless otherwise noted, the method is the one described by Press et al. (1992), which is based on an iterative process to minimize  $\chi^2$ , taking into account the uncertainties in both coordinates. In some of our data, the uncertainties are asymmetric (e.g., as a result of the FR/RSS method and the use of the CCPD), and since the fitting method does not account for this, we use the mean of the positive and negative uncertainty estimates in a given coordinate for each data point. We find that similar results are obtained when using the Pearson linear correlation and the Spearman rank-order correlation. We present below only Pearson coefficients.

<sup>6</sup>Koratkar & Gaskell (1991a) show the effects of calculating the centroid at various levels of the peak value. The ICCFs presented here are smoother than those presented in their study. Therefore, a level chosen at 80% of the peak should be adequate.

TABLE 3  
CONTINUUM LIGHT CURVES

JD	$f_{\lambda}^a$
PG 0026	
2448461.5	$22.48 \pm 0.36$
2448490.6	$20.30 \pm 0.30$
2448520.3	$19.59 \pm 0.56$
2448545.8	$20.11 \pm 0.15$
2448769.6	$21.12 \pm 1.20$
2448836.5	$23.88 \pm 0.74$
2448869.4	$23.02 \pm 0.64$
2448890.4	$24.51 \pm 0.31$
2448925.2	$23.83 \pm 0.58$
2448949.4	$25.73 \pm 0.46$

<sup>a</sup>In units of  $10^{-16}$  ergs s<sup>-1</sup> cm<sup>-2</sup> Å<sup>-1</sup>.

Note.—Table 3 is presented in its entirety in the electronic edition of the *Astrophysical Journal*. A portion is shown here for guidance regarding its form and content.

TABLE 4  
BALMER LINE LIGHT CURVES

JD	Flux <sup>a</sup>
PG 0026 - H $\alpha$	
2448836.5	$44.50 \pm 2.56$
2448890.4	$49.02 \pm 1.60$
2448949.4	$60.81 \pm 1.56$
2448988.6	$53.46 \pm 0.71$
2449218.6	$51.81 \pm 1.57$
2449220.5	$54.04 \pm 0.99$
2449248.4	$48.81 \pm 1.03$
2449250.5	$57.43 \pm 1.14$
2449278.6	$53.72 \pm 2.00$
2449281.7	$62.68 \pm 0.70$

<sup>a</sup>In units of  $10^{-14}$  ergs s<sup>-1</sup> cm<sup>-2</sup>.

Note.—Table 4 is presented in its entirety in the electronic edition of the *Astrophysical Journal*. A portion is shown here for guidance regarding its form and content.

TABLE 5  
VARIABILITY MEASURE  $\sigma_N$

Object	Cont <sup>a</sup>	H $\alpha$	H $\beta$	H $\gamma$
PG 0026	14.7	9.3	8.0	8.4
PG 0052	17.6	10.1	11.4	20.2
PG 0804	18.2	5.8	6.2	8.7
PG 0844	10.1	6.7	9.7	10.0
PG 0953	13.3	...	5.5	6.2
PG 1211	16.2	10.3	12.2	12.8
PG 1226	11.9	7.7	7.8	12.3
PG 1229	10.9	8.1	12.5	17.9
PG 1307	9.8	7.9	12.8	14.3
PG 1351	9.8	4.0	4.7	...
PG 1411	8.5	3.4	5.1	2.8
PG 1426	15.3	7.0	8.8	...
PG 1613	12.4	5.6	6.1	...
PG 1617	17.3	7.4	11.5	...
PG 1700	6.8	...	3.2	...
PG 1704	14.5	...	10.7	18.0
PG 2130	9.3	6.2	8.9	8.9

<sup>a</sup>Continuum at rest wavelength  $\sim$ 5100 Å (see Table 2 column [7] for exact wavelength intervals).

TABLE 6  
CROSS-CORRELATION RESULTS, VELOCITY MEASUREMENTS, AND FLUXES

Object	line	$\tau_{cent}$ (days)	$\tau_{peak}$ (days)	$r_{max}$	Number Obs.	$v_{FWHM}$ (mean) km s $^{-1}$	$v_{FWHM}$ (rms) km s $^{-1}$	Flux $10^{-14}$ ergs s $^{-1}$ cm $^{-2}$
(1)	(2)	(3)	(4)	(5)	(6)	(7)	(8)	(9)
PG 0026	H $\alpha$	132 $^{+29}_{-31}$	108 $^{+63}_{-47}$	0.81	55	1527 $\pm$ 99	1179 $\pm$ 76	59.0 $\pm$ 5.6
PG 0026	H $\beta$	125 $^{+29}_{-36}$	85 $^{+36}_{-28}$	0.84	53	2100 $\pm$ 140	1358 $\pm$ 91	12.7 $\pm$ 1.1
PG 0052	H $\alpha$	211 $^{+66}_{-44}$	193 $^{+85}_{-93}$	0.68	53	2690 $\pm$ 510	3280 $\pm$ 630	74.6 $\pm$ 7.9
PG 0052	H $\beta$	99 $^{+30}_{-31}$	75 $^{+22}_{-15}$	0.75	56	3990 $\pm$ 240	4550 $\pm$ 270	18.0 $\pm$ 2.1
PG 0052	H $\gamma$	90 $^{+27}_{-20}$	69 $^{+19}_{-9}$	0.74	56	4050 $\pm$ 300	5120 $\pm$ 380	8.2 $\pm$ 1.8
PG 0804	H $\alpha$	193 $^{+20}_{-17}$	187 $^{+29}_{-37}$	0.83	70	2757 $\pm$ 55	2909 $\pm$ 58	209 $\pm$ 12
PG 0804	H $\beta$	151 $^{+26}_{-24}$	118 $^{+34}_{-30}$	0.85	70	2984 $\pm$ 51	2430 $\pm$ 42	64.5 $\pm$ 4.2
PG 0804	H $\gamma$	108 $^{+39}_{-38}$	82 $^{+67}_{-46}$	0.74	67	3120 $\pm$ 150	2470 $\pm$ 120	22.4 $\pm$ 2.4
PG 0844	H $\alpha$	39 $^{+16}_{-16}$	37 $^{+19}_{-24}$	0.74	46	2210 $\pm$ 100	2700 $\pm$ 120	95.3 $\pm$ 6.5
PG 0844	H $\beta$	13 $^{+14}_{-11}$ a	10 $^{+20}_{-19}$	0.79	48	2730 $\pm$ 120	2830 $\pm$ 120	30.2 $\pm$ 3.0
PG 0844	H $\gamma$	31 $^{+77}_{-49}$	28 $^{+89}_{-43}$	0.58	45	3210 $\pm$ 360	4770 $\pm$ 530	13.0 $\pm$ 1.9
PG 0953	H $\beta$	187 $^{+27}_{-33}$	207 $^{+22}_{-26}$	0.72	35	2885 $\pm$ 65	2723 $\pm$ 62	15.97 $\pm$ 0.93
PG 0953	H $\gamma$	203 $^{+36}_{-59}$	213 $^{+24}_{-73}$	0.54	34	3110 $\pm$ 130	3860 $\pm$ 160	7.12 $\pm$ 0.56
PG 1211	H $\alpha$	116 $^{+38}_{-46}$	69 $^{+123}_{-33}$	0.87	37	1479 $\pm$ 74	1051 $\pm$ 53	192 $\pm$ 20
PG 1211	H $\beta$	103 $^{+32}_{-44}$	28 $^{+142}_{-26}$	0.87	36	1832 $\pm$ 81	1479 $\pm$ 66	54.5 $\pm$ 6.7
PG 1211	H $\gamma$	145 $^{+66}_{-47}$	117 $^{+120}_{-68}$	0.86	34	2380 $\pm$ 150	2200 $\pm$ 140	27.3 $\pm$ 3.9
PG 1226	H $\alpha$	514 $^{+65}_{-64}$	447 $^{+181}_{-65}$	0.71	34	2810 $\pm$ 190	1330 $\pm$ 88	601 $\pm$ 48
PG 1226	H $\beta$	382 $^{+117}_{-96}$	342 $^{+145}_{-89}$	0.78	39	3416 $\pm$ 72	2742 $\pm$ 58	172 $\pm$ 14
PG 1226	H $\gamma$	307 $^{+57}_{-86}$	306 $^{+52}_{-61}$	0.79	39	3760 $\pm$ 170	3440 $\pm$ 160	61.1 $\pm$ 8.7
PG 1229	H $\alpha$	71 $^{+39}_{-46}$	48 $^{+85}_{-10}$	0.78	32	2960 $\pm$ 110	3350 $\pm$ 130	74.7 $\pm$ 6.1
PG 1229	H $\beta$	36 $^{+32}_{-18}$	20 $^{+10}_{-20}$	0.80	33	3440 $\pm$ 120	3490 $\pm$ 120	19.8 $\pm$ 2.5
PG 1229	H $\gamma$	16 $^{+27}_{-39}$	7 $^{+36}_{-49}$	0.81	29	3400 $\pm$ 330	3000 $\pm$ 290	7.8 $\pm$ 1.5
PG 1307	H $\alpha$	179 $^{+94}_{-145}$	228 $^{+97}_{-169}$	0.67	20	3690 $\pm$ 140	3280 $\pm$ 120	73.9 $\pm$ 6.0
PG 1307	H $\beta$ <sup>b</sup>	108 $^{+46}_{-115}$	32 $^{+49}_{-96}$	0.59	23	4190 $\pm$ 210	5260 $\pm$ 270	19.2 $\pm$ 2.6
PG 1307	H $\gamma$	201 $^{+72}_{-168}$	252 $^{+105}_{-426}$	0.64	23	4030 $\pm$ 240	3400 $\pm$ 200	7.4 $\pm$ 1.3
PG 1351	H $\alpha$	247 $^{+162}_{-78}$	258 $^{+286}_{-76}$	0.49	29	1170 $\pm$ 160	950 $\pm$ 130	76.9 $\pm$ 3.2
PG 1411	H $\alpha$	103 $^{+40}_{-37}$	71 $^{+17}_{-18}$	0.87	24	2172 $\pm$ 57	2135 $\pm$ 56	133.0 $\pm$ 4.6
PG 1411	H $\beta$	118 $^{+72}_{-71}$	67 $^{+157}_{-31}$	0.64	24	2456 $\pm$ 96	2740 $\pm$ 110	33.3 $\pm$ 1.8
PG 1426	H $\alpha$	90 $^{+46}_{-52}$	66 $^{+56}_{-59}$	0.87	20	5450 $\pm$ 150	4850 $\pm$ 130	136.2 $\pm$ 9.6
PG 1426	H $\beta$	115 $^{+49}_{-68}$	61 $^{+81}_{-66}$	0.83	20	6250 $\pm$ 390	5520 $\pm$ 340	30.9 $\pm$ 2.9
PG 1613	H $\alpha$	43 $^{+40}_{-22}$	35 $^{+185}_{-26}$	0.43	44	6060 $\pm$ 210	1598 $\pm$ 56	97.0 $\pm$ 5.8
PG 1613	H $\beta$	44 $^{+20}_{-23}$	29 $^{+36}_{-31}$	0.43	48	7000 $\pm$ 380	2500 $\pm$ 140	20.2 $\pm$ 1.3
PG 1617	H $\alpha$	111 $^{+31}_{-37}$	83 $^{+45}_{-32}$	0.80	32	4270 $\pm$ 410	3160 $\pm$ 300	50.4 $\pm$ 3.9
PG 1617	H $\beta$	78 $^{+30}_{-41}$	83 $^{+32}_{-55}$	0.75	34	5120 $\pm$ 850	3880 $\pm$ 650	14.0 $\pm$ 1.7
PG 1617	H $\gamma$	43 $^{+117}_{-58}$	50 $^{+148}_{-49}$	0.67	32	3100 $\pm$ 750	3110 $\pm$ 750	4.2 $\pm$ 1.1
PG 1700	H $\beta$	114 $^{+246}_{-235}$ a	14 $^{+296}_{-177}$	0.54	37	2180 $\pm$ 170	1970 $\pm$ 150	18.88 $\pm$ 0.99
PG 1704	H $\beta$	437 $^{+252}_{-391}$	527 $^{+263}_{-407}$	0.43	24	890 $\pm$ 280	400 $\pm$ 120	3.18 $\pm$ 0.41
PG 2130	H $\alpha$	237 $^{+53}_{-28}$	194 $^{+252}_{-33}$	0.59	64	2022 $\pm$ 88	2236 $\pm$ 97	168 $\pm$ 11
PG 2130	H $\beta$	188 $^{+136}_{-27}$	186 $^{+144}_{-103}$	0.66	64	2410 $\pm$ 150	3010 $\pm$ 180	51.2 $\pm$ 4.6
PG 2130	H $\gamma$	196 $^{+130}_{-46}$	218 $^{+104}_{-102}$	0.72	54	2850 $\pm$ 190	3050 $\pm$ 210	22.7 $\pm$ 2.7

<sup>a</sup>Computed from all points within 60% of the peak value,  $r_{max}$ , due to the noisiness of the data.

<sup>b</sup>The peak of the ICCF measured is the one consistent with the ZDCF results and with the H $\alpha$  and H $\gamma$  results.

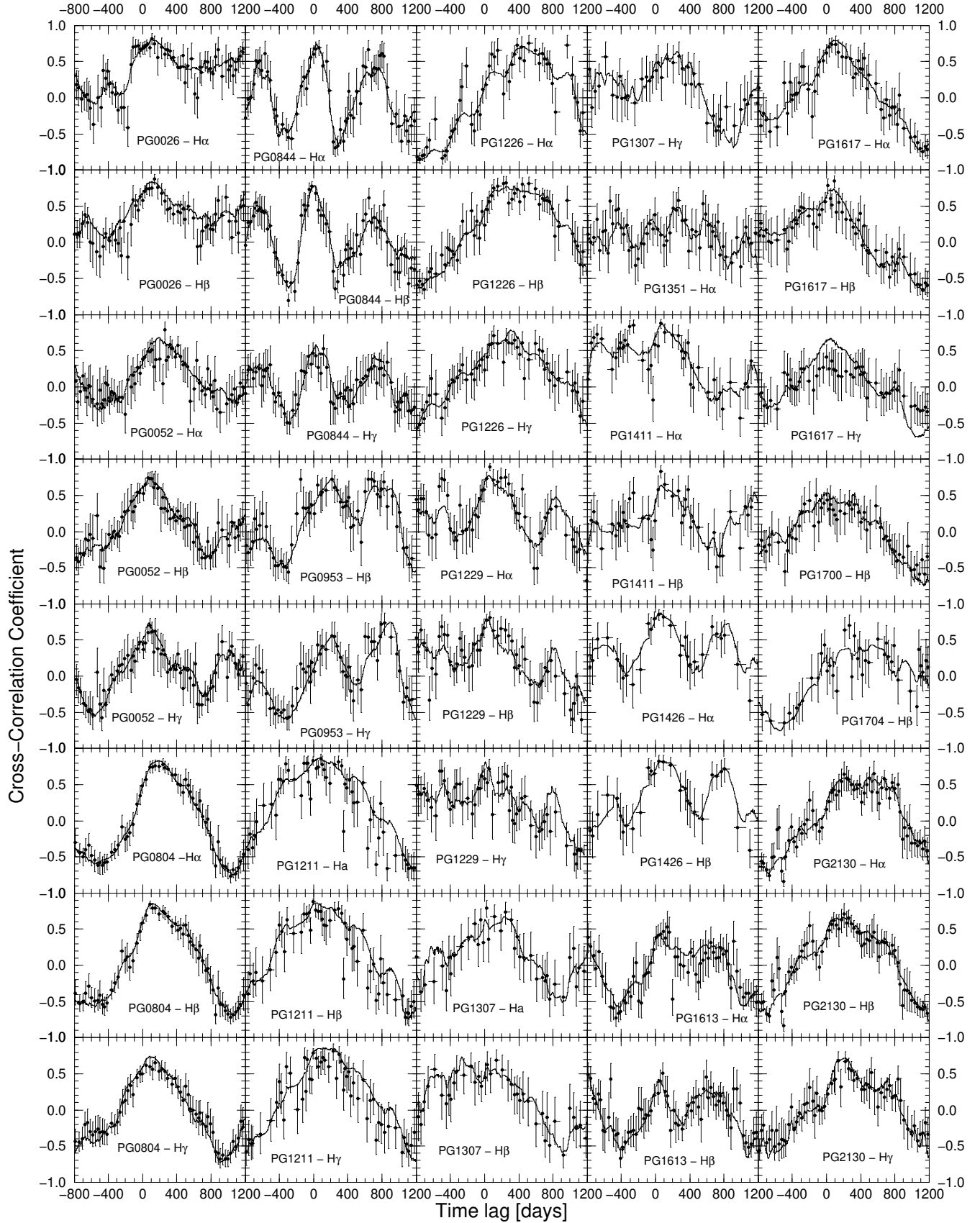


FIG. 4.— Cross correlation functions: ICCF (solid line) and ZDCF (circles with error bars) for all emission lines with peak correlation coefficients  $> 0.4$ . See text and Table 6 for details.

#### 4.1. The Size of the BLR

Caution must be exercised when using time lags to estimate BLR sizes because there are various assumptions and complications involved:

1. The CCF is sensitive to the characteristics of the continuum variation, since it is a convolution of the transfer function and the continuum autocorrelation function (Penston 1991; Peterson 1993). Hence, there is a dependence of the peak and centroid of the CCF on the nature of the continuum variability. An illustration of this dependence is given by Netzer & Maoz (1990).
2. A real change in BLR size and geometry, over the 7 year period, is not out of the question. Using the time-lags measured here, and the observed FWHMs, we deduce a dynamical (crossing) time of the order of 30 years for the more luminous objects and about a year for the lowest luminosity Seyfert galaxies.
3. The measured time lag can be affected by the nonlinear response of some emission-line intensities to continuum variations. Nonlinear responses are suggested by various studies (O'Brien, Goad, & Gondhalekar, 1995; Shields, Ferland, & Peterson, 1995) and discussed by Kaspi & Netzer (1999).
4. The ionizing continuum variations may behave differently from the observed optical continuum. Due to anisotropic continuum emission, the emission line gas may be illuminated by an ionizing continuum that is poorly represented by the observed optical continuum (e.g. Netzer 1987). Furthermore, variable beaming or obscuration may be different along the different lines of sight from the continuum source to the observer and to the gas. Most studies show the continuum varies in phase with little or no time delay (albeit, with smaller amplitude at longer wavelengths) over a wide wavelength range. There are, however, some exceptions (e.g., Peterson et al. 1998b) and it is clear that a full understanding of the continuum emission processes is yet to be obtained. An extreme example is shown by Nandra et al. (1998) who found that the X-ray and UV continuum are not strongly correlated at zero time lag in NGC 7469, with some X-ray emission peaks lagging behind the UV peaks by  $\sim 4$  days. Recently, Maoz, Edelson, & Nandra (2000) have demonstrated even weaker correlation at zero lag between X-ray and optical variations in NGC 3516.
5. For a given object, different lines from different ions have different time lags. Thus, considering the entire sample, the same emission lines should be used in all objects. Balmer lines are useful since their lag has been measured in most AGN where reverberation mapping has been attempted. However, as argued by Kaspi & Netzer (1999), the theoretical modeling of these lines is very uncertain and they are useful mostly because they provide a uniform base for comparing low luminosity Seyferts with high luminosity quasars.
6. There may be flux contributions by other emission lines blended with the Balmer lines. These emission lines may

have a different time lag and affect the measured emission line lag. An example of this potential situation is the variable Fe II emission lines near  $H\beta$ .

A possible manifestation of some of these difficulties is the fact that for some objects, different monitoring campaigns result in different time lags. The effect was first noted in the  $H\beta$  time lags found by Peterson et al. (1991;  $\sim 7$  days) and Netzer et al. (1990;  $\sim 20$  days) for the Seyfert galaxy NGC 5548. Other examples are the longer time lag deduced for PG 0804 and PG 0953 in this paper, compared with Paper II (see above), and the different time lags in each observing season for NGC 5548 (Peterson et al. 1999).

Bearing in mind the above points, we convert the time lags (deduced from the ICCF centroid,  $\tau_{cent}$  from Table 6) of the Balmer emission lines directly into BLR sizes (hereafter  $R_{BLR}$ ) after applying a cosmological  $(1+z)^{-1}$  factor. We find that time lags derived from multiple Balmer lines are consistent with each other for individual quasars. The derived linear relations are:

$$R_{BLR}(H\alpha) = (1.19 \pm 0.23)R_{BLR}(H\beta) + (13 \pm 19) , \quad (2)$$

and

$$R_{BLR}(H\gamma) = (0.96 \pm 0.30)R_{BLR}(H\beta) - (3 \pm 33) , \quad (3)$$

i.e., both are consistent with a slope of 1.0 and a zero intercept. In view of this, we adopt the mean time lag measured for  $H\alpha$  and  $H\beta$  as the best estimate of  $R_{BLR}$ <sup>7</sup>. The relatively low equivalent width of  $H\gamma$  makes it more difficult to measure and we do not include it in the estimate of BLR size. In several objects only one of  $H\alpha$  or  $H\beta$  is available and we thus use a single line. For the Seyfert 1s we use the  $H\beta$  time lags from Wandel et al. (1999) and correct them by the  $(1+z)^{-1}$  factor. We have used the same method for calculating the time lags as that used by Wandel et al. (1999). Values for  $R_{BLR}$  for all objects are listed in Table 7, column (2).

#### 4.2. Luminosity Determination

The exact shape of the spectral energy distribution (SED) of most objects in our sample is unknown. Furthermore, much of this luminosity is emitted in the unobservable far UV and there are still unsolved fundamental issues concerning the shape of the continuum (e.g., Zheng et al. 1997, Laor et al. 1997, and references therein). Even in those cases where multiwavelength data exist, the data are generally obtained at different epochs, and variability may render a simple integration over a wide wavelength range inappropriate. (See also a discussion by Dumont, Collin-Souffrin, & Nazarova; 1998, that demonstrates how poorly the SED is determined for even one of the best-studied AGN, NGC 5548.) Intrinsic reddening and possible orientation effects complicate the situation and it is thus unclear what fraction of the total luminosity we are sampling.

An additional complication is the contribution of the host galaxy to the luminosity of the nucleus. While in high-luminosity AGN this contribution is negligible, this is not the case in low-luminosity objects. Determining the host galaxy flux within a given spectrograph aperture is a complicated task, attempted only in a few cases (e.g., Peterson et al. 1995). The implementation of such corrections is beyond the scope of this paper.

<sup>7</sup>When using only  $H\beta$  for the analysis, we derive the same results but with somewhat larger scatter.

TABLE 7  
RADII, LUMINOSITIES, & MASSES

Object (1)	$R_{BLR}$ (lt-days) (2)	$\lambda L_\lambda(5100\text{\AA})$ $10^{44} \text{ ergs s}^{-1}$ (3)	$M(\text{mean})$ $10^7 M_\odot$ (4)	$M(\text{rms})$ $10^7 M_\odot$ (5)
3C 120	$42^{+27}_{-20}$	$0.73 \pm 0.13$	$2.3^{+1.5}_{-1.1}$	$3.0^{+1.9}_{-1.4}$
3C 390.3	$22.9^{+6.3}_{-8.0}$	$0.64 \pm 0.11$	$34^{+11}_{-13}$	$37^{+12}_{-14}$
Akn 120	$37.4^{+3.1}_{-6.3}$	$1.39 \pm 0.26$	$18.4^{+3.9}_{-4.3}$	$18.7^{+4.0}_{-4.4}$
F9	$16.3^{+3.3}_{-7.6}$	$1.37 \pm 0.15$	$8.0^{+2.4}_{-4.1}$	$8.3^{+2.5}_{-4.3}$
IC 4329A	$1.4^{+3.3}_{-2.9}$	$0.164 \pm 0.021$	$0.5^{+1.3}_{-1.1}$	$0.7^{+1.8}_{-1.6}$
Mrk 79	$17.7^{+4.8}_{-8.4}$	$0.423 \pm 0.056$	$5.2^{+2.0}_{-2.8}$	$10.2^{+3.9}_{-5.6}$
Mrk 110	$18.8^{+6.3}_{-6.6}$	$0.38 \pm 0.13$	$0.56^{+0.20}_{-0.21}$	$0.77^{+0.28}_{-0.29}$
Mrk 335	$16.4^{+5.1}_{-3.2}$	$0.622 \pm 0.057$	$0.63^{+0.23}_{-0.17}$	$0.38^{+0.14}_{-0.10}$
Mrk 509	$76.7^{+6.3}_{-6.0}$	$1.47 \pm 0.25$	$5.78^{+0.68}_{-0.66}$	$9.2^{+1.1}_{-1.1}$
Mrk 590	$20.0^{+4.4}_{-2.9}$	$0.510 \pm 0.096$	$1.78^{+0.44}_{-0.33}$	$1.38^{+0.34}_{-0.25}$
Mrk 817	$15.0^{+4.2}_{-3.4}$	$0.526 \pm 0.077$	$4.4^{+1.3}_{-1.1}$	$3.54^{+1.03}_{-0.86}$
NGC 3227	$10.9^{+5.6}_{-10.9}$	$0.0202 \pm 0.0011$	$3.9^{+2.1}_{-3.9}$	$4.9^{+2.6}_{-4.9}$
NGC 3783	$4.5^{+3.6}_{-3.1}$	$0.177 \pm 0.015$	$0.94^{+0.92}_{-0.84}$	$1.10^{+1.07}_{-0.98}$
NGC 4051	$6.5^{+6.6}_{-4.1}$	$0.00525 \pm 0.00030$	$0.13^{+0.13}_{-0.08}$	$0.14^{+0.15}_{-0.09}$
NGC 4151	$3.0^{+1.8}_{-1.4}$	$0.0720 \pm 0.0042$	$1.53^{+1.06}_{-0.89}$	$1.20^{+0.83}_{-0.70}$
NGC 5548	$21.2^{+2.4}_{-0.7}$	$0.270 \pm 0.053$	$12.3^{+2.3}_{-1.8}$	$9.4^{+1.7}_{-1.4}$
NGC 7469	$4.9^{+0.6}_{-1.1}$	$0.553 \pm 0.016$	$0.65^{+0.64}_{-0.65}$	$0.75^{+0.74}_{-0.75}$
PG 0026	$113^{+18}_{-21}$	$7.0 \pm 1.0$	$5.4^{+1.0}_{-1.1}$	$2.66^{+0.49}_{-0.55}$
PG 0052	$134^{+31}_{-23}$	$6.5 \pm 1.1$	$22.0^{+6.3}_{-5.3}$	$30.2^{+8.8}_{-7.4}$
PG 0804	$156^{+15}_{-13}$	$6.6 \pm 1.2$	$18.9^{+1.9}_{-1.7}$	$16.3^{+1.6}_{-1.5}$
PG 0844	$24.2^{+10.0}_{-9.1}$	$1.72 \pm 0.17$	$2.16^{+0.90}_{-0.83}$	$2.7^{+1.1}_{-1.0}$
PG 0953	$151^{+22}_{-27}$	$11.9 \pm 1.6$	$18.4^{+2.8}_{-3.4}$	$16.4^{+2.5}_{-3.0}$
PG 1211	$101^{+23}_{-29}$	$4.93 \pm 0.80$	$4.05^{+0.96}_{-1.21}$	$2.36^{+0.56}_{-0.70}$
PG 1226	$387^{+58}_{-50}$	$64.4 \pm 7.7$	$55.0^{+8.9}_{-7.9}$	$23.5^{+3.7}_{-3.3}$
PG 1229	$50^{+24}_{-23}$	$0.94 \pm 0.10$	$7.5^{+3.6}_{-3.5}$	$8.6^{+4.1}_{-4.0}$
PG 1307	$124^{+45}_{-80}$	$5.27 \pm 0.52$	$28^{+11}_{-18}$	$33^{+12}_{-22}$
PG 1351	$227^{+149}_{-72}$	$4.38 \pm 0.43$	$4.6^{+3.2}_{-1.9}$	$3.0^{+2.1}_{-1.3}$
PG 1411	$102^{+38}_{-37}$	$3.25 \pm 0.28$	$8.0^{+3.0}_{-2.9}$	$8.8^{+3.3}_{-3.2}$
PG 1426	$95^{+31}_{-39}$	$4.09 \pm 0.63$	$47^{+16}_{-20}$	$37^{+13}_{-16}$
PG 1613	$39^{+20}_{-14}$	$6.96 \pm 0.87$	$24.1^{+12.5}_{-8.9}$	$2.37^{+1.23}_{-0.88}$
PG 1617	$85^{+19}_{-25}$	$2.37 \pm 0.41$	$27.3^{+8.3}_{-9.7}$	$15.4^{+4.8}_{-5.5}$
PG 1700	$88^{+190}_{-182}$	$27.1 \pm 1.9$	$6^{+13}_{-13}$	$5.0^{+11}_{-10}$
PG 1704	$319^{+184}_{-285}$	$35.6 \pm 5.2$	$3.7^{+3.1}_{-4.0}$	$0.75^{+0.63}_{-0.81}$
PG 2130	$200^{+67}_{-18}$	$2.16 \pm 0.20$	$14.4^{+5.1}_{-1.7}$	$20.2^{+7.1}_{-2.4}$

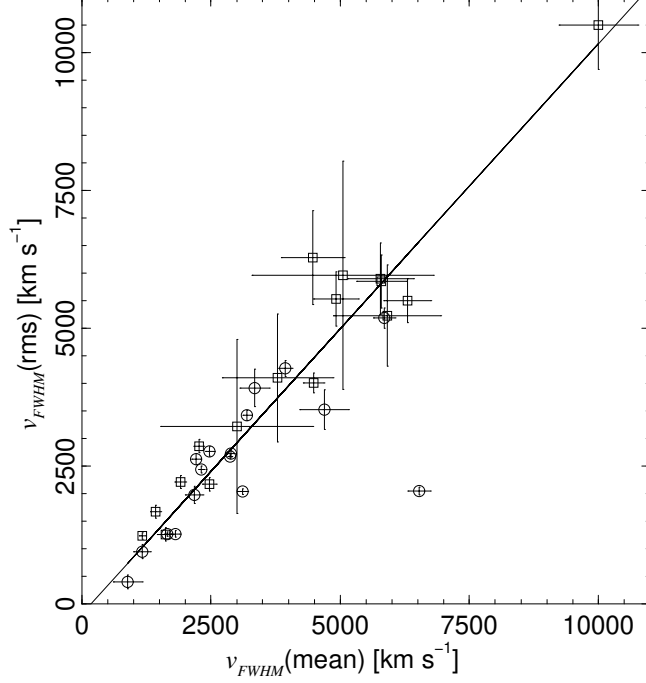


FIG. 5.—  $v_{FWHM}(rms)$  vs.  $v_{FWHM}(mean)$ . In this and subsequent figures, PG quasars are denoted by circles and Seyfert 1s are denoted by squares. The solid line is the best fit to the data. The outlier is PG 1613, which apparently varies only in the core of its very broad lines. The object with the broadest lines is 3C 390.3.

Following Wandel et al. (1999), we use  $\lambda L_\lambda$  at 5100 Å (rest frame) as our luminosity measure. This luminosity is calculated assuming zero cosmological constant, deceleration parameter  $q_0 = 0.5$ , and Hubble constant  $H_0 = 75 \text{ km s}^{-1} \text{Mpc}^{-1}$  (note that these values are different from the ones used by Wandel et al. 1999). This monochromatic luminosity can be translated into an integrated 0.1–1  $\mu\text{m}$  luminosity, assuming a power-law continuum of the form  $f_\nu \propto \nu^{-0.5}$ , as in Papers I & II, by applying a correction factor of 3.1. For the 5100 Å point, we use the continuum measurement on the red side of H $\beta$  (see wavelength ranges in column (7) of Table 2). The uncertainty in this value is taken to be only due to the variation range of each object, and is represented by the rms of the light curve. The observed flux has been corrected for Galactic extinction using the  $A_B$  values from NED<sup>8</sup> (see Table 1 column [7]) and a standard extinction curve (Savage & Mathis 1979). Monochromatic luminosities,  $\lambda L_\lambda$ (5100 Å), are listed in Table 7, column (3).

We have also tried an alternative process to determine the optical luminosity. Using line-free bands in the optical spectra, we have fitted a continuum to the mean and rms spectra of all objects. We integrated those continua over the rest frame wavelength of 4500–6000 Å to obtain the mean luminosity and its range. We have found the results to be very similar to those obtained by using the monochromatic luminosity. We have also examined the consequences of using the H $\beta$  luminosity (rather than the optical luminosity) to represent the ionizing luminosity of each AGN. Here too, we have found the results presented below to be mostly unchanged by this choice. Below we use only  $\lambda L_\lambda$ (5100 Å) as our luminosity measure.

#### 4.3. Mass Determination

To estimate the central masses of the quasars we need to assume gravitationally dominated motions of the BLR clouds

( $M \approx G^{-1}v^2r$ ). This assumption is presented in Gaskell (1988) for the Seyfert 1 galaxy NGC 4151 and is also discussed and justified by Wandel et al. (1999) and Peterson & Wandel (1999) for the Seyfert 1 galaxy NGC 5548 (though see Gaskell 1996 for a more general approach). There are, however, several complications regarding the velocity field. Although it is generally believed that the line widths represent a Keplerian velocity, it is not clear how to convert the observed profile into a velocity measure, since the observed profiles are different from the ones expected from simple Keplerian orbits of arbitrary inclinations. In the absence of such information, it is common to use the rest-frame FWHM of the emission line. Because the broad emission lines of AGN are composed of a narrow component superposed on a broader components, a unique FWHM determination is not straightforward. In particular, deblending the components is complicated since the line profiles cannot be represented by simple analytical functions. Also, the line profiles and widths are variable as is evident, for example, in Gilbert et al. (1999) and from the spectra obtained in this study. These variations can be due to a real change in the BLR velocity field, or other reasons, such as blending with weak lines, or observational effects (e.g., inaccurate wavelength calibration, or changes in the seeing).

We use two different methods to estimate a typical velocity. In the first method, for each quasar we measure the FWHM of each line in all the spectra and calculate the mean FWHM,  $v_{FWHM}(\text{mean})$ , and its uncertainty (rms). This empirical way of estimating the scatter accounts for all the uncertainties involved, such as spectral resolution, pixelation of the line profile, and uncertainties in continuum determination. The values are listed in Table 6, column (7).

The second method, proposed by Peterson et al. (1998a), uses the rms spectrum to compute the FWHM of the lines. In

<sup>8</sup>The NASA/IPAC Extragalactic Database (NED) is operated by the Jet Propulsion Laboratory, California Institute of Technology, under contract with the National Aeronautics and Space Administration.

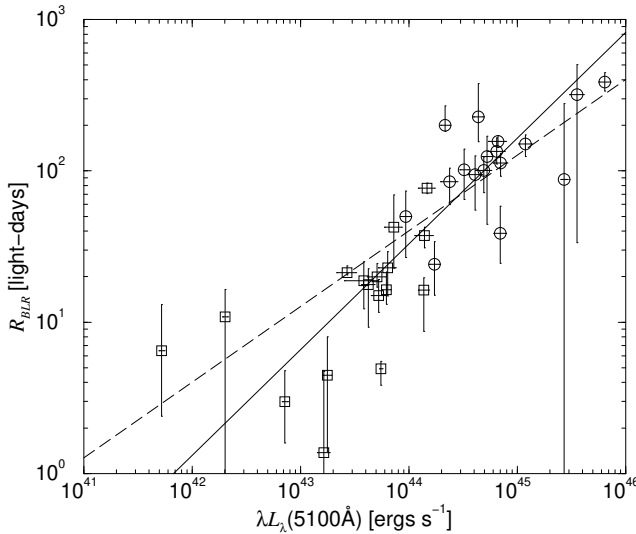


FIG. 6.— BLR size—luminosity relation. The solid line is the best fit to the data. The dashed line is a fit with a slope of 0.5.

principle, constant features in the mean spectrum (such as narrow forbidden emission lines, narrow components of the permitted emission lines, galactic absorptions, and constant continuum and broad-line features) are excluded in this method. The FWHM measures only the part of the line that varied and thus corresponds to the  $R_{BLR}$  measured from the reverberation mapping<sup>9</sup>. For the rms spectrum of each object we have listed the emission lines' FWHM,  $v_{FWHM}(\text{rms})$ , in column (8) of Table 6. There is no simple way to determine the uncertainty of  $v_{FWHM}(\text{rms})$ , and instead we have used the relative uncertainty in  $v_{FWHM}(\text{mean})$ .

Like the time lags derived using H $\alpha$  and H $\beta$ , the FWHM of all lines for a given object are consistent with each other. Thus, for the PG quasars we use the average FWHM of H $\alpha$  and H $\beta$ . For the Seyfert 1 galaxies we have used the mean and rms FWHM quoted in Wandel et al. (1999). The FWHM from the rms spectrum versus the mean FWHM from all spectra is plotted in Fig. 5. We find the correlation to be highly significant with correlation coefficient of 0.888. A linear fit gives the relation

$$v_{FWHM}(\text{rms}) = (1.035 \pm 0.034)v_{FWHM}(\text{mean}) - (185 \pm 93) , \quad (4)$$

which is plotted as the solid line in Fig. 5. The two velocity estimates are similar and Peterson et al.'s (1998a) preference for the FWHM determined from the rms spectra is not empirically justified. However, in the subsequent analysis we will use both estimates of the broad-line FWHM for each object.

To determine  $v$  we correct  $v_{FWHM}$  by a factor of  $\sqrt{3}/2$ , to account for velocities in three dimensions and for using half of the FWHM. The virial “reverberation” mass is then:

$$M = 1.464 \times 10^5 \left( \frac{R_{BLR}}{\text{lt days}} \right) \left( \frac{v_{FWHM}}{10^3 \text{ km s}^{-1}} \right)^2 M_{\odot} . \quad (5)$$

The results of this calculation are listed in columns (4) and (5) of Table 7 for  $v_{FWHM}(\text{mean})$  and  $v_{FWHM}(\text{rms})$ , respectively.

## 5. DISCUSSION

### 5.1. Size—Luminosity Relation

The  $R_{BLR}$ —luminosity relation is presented in Fig. 6. The correlation coefficient is 0.827, and its significance level is  $1.7 \times 10^{-9}$ . A linear fit to the points gives

$$R_{BLR} = (32.9_{-1.9}^{+2.0}) \left( \frac{\lambda L_{\lambda}(5100 \text{ \AA})}{10^{44} \text{ ergs s}^{-1}} \right)^{0.700 \pm 0.033} \text{ lt days} \quad (6)$$

(solid line plotted in Fig. 6). Considering the Seyfert nuclei ( $\log(\lambda L_{\lambda}(5100 \text{ \AA})) \lesssim 44.2$ ), or the PG quasars alone, we find only marginally significant correlations, probably because of the narrow luminosity ranges. A significant correlation emerges only when using the whole luminosity range.

The present result is remarkable for two reasons. First, earlier studies of this kind found a smaller power-law index in the BLR size—AGN luminosity relation (closer to 0.5, e.g., Koratkar & Gaskell 1991b; Wandel et al. 1999). A line with this slope was fit to the data and is shown as a dashed line in Fig. 6. Our result using the combined sample is not consistent with previous results. Second, under the assumptions that the shape of the ionizing continuum in AGN is independent of  $L$ , and that all AGN are characterized by the same ionization parameter and BLR density (as suggested by the similar line ratios in low- and high-luminosity sources), one expects  $R_{BLR} \propto L^{0.5}$ . The theoretical prediction is based on the assumption that the gas distribution, and hence the mean BLR size, scales with the strength of the radiation field. Our present result suggests that those assumptions should be re-examined. This is also implied from recent models (e.g., Kaspi & Netzer 1999 and references therein) which show a wide distribution of properties (such as BLR density, column density, and ionization parameter) across the BLR of a single active nucleus. Therefore, a range of properties may also exist among different AGN, and the above assumptions of uniform ionization parameter and BLR density for all AGN is likely incorrect. If an effective ionization parameter can be defined, our result suggests that it may be a decreasing function of luminosity.

<sup>9</sup>The rms spectra shown by Peterson et al. (1998a) often show narrow forbidden line residuals that are probably due to variable seeing and small shifts in wavelength calibration. We see the same effect in our rms spectra as well. It is likely that the same effect operates on the narrow component of the Balmer lines, and therefore, the rms spectra are also not completely free of constant narrow components. The degree of this contamination may vary from object to object.

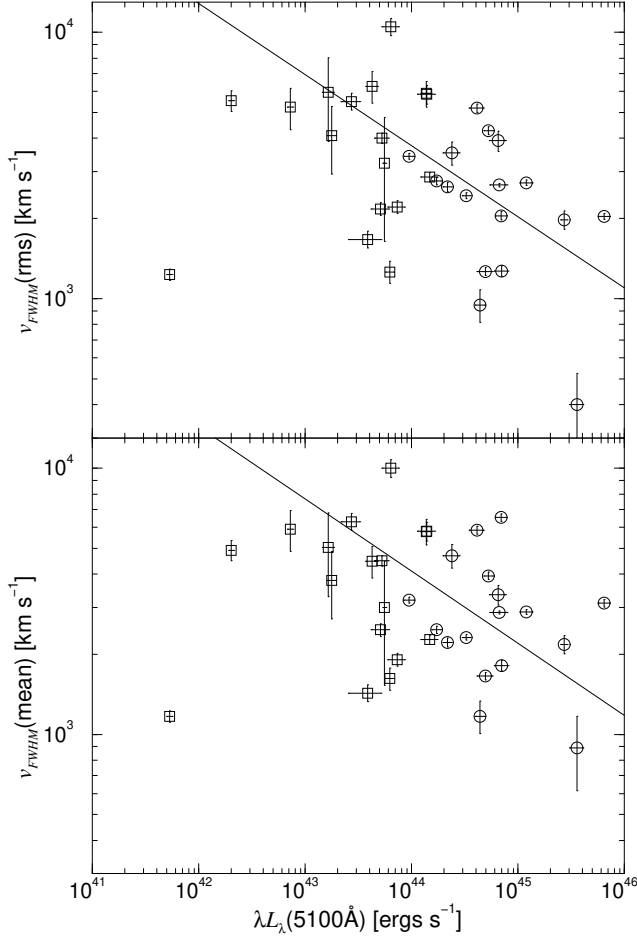


FIG. 7.—FWHM—luminosity relations. Top: FWHM derived from the rms spectrum of each object. Bottom: FWHM derived from averaging the FWHMs in all spectra for a given object. Solid lines are the best fit to the data after excluding the outlier at the lowest luminosity (NGC 4051).

### 5.2. FWHM—Luminosity Relation

Our sample allows us to re-address the issue of the velocity—luminosity relation in AGN. Shuder (1984) noted that the FWHM of the Balmer lines increases with luminosity for a sample of 25 AGN. Wandel & Yahil (1985) found a correlation coefficient of 0.5 between the H $\beta$  full width at zero intensity (FWOI) and the 4000 Å continuum luminosity for a literature compilation of 94 AGN. Joly et al. (1985; and references therein) also reported a weak correlation between the FWOI of H $\beta$  and the optical luminosity in a similar collection of objects. Boroson & Green (1992) note the FWOI of H $\beta$  is quite sensitive to noise and depends strongly on the quality of the Fe II subtraction. These authors found an anticorrelation coefficient of  $-0.275$  between the H $\beta$  FWHM and absolute  $V$  magnitude, significant at the 99% confidence level, in a sample of 87 PG quasars. In a recent work Stirpe, Robinson, & Axon (1999) measured H $\alpha$  velocities for 126 AGN and found them to weakly correlate with the luminosity.

In addressing the issue of the velocity—luminosity relation we note that our sample is *not* complete, especially with the inclusion of the heterogeneous Seyfert sample. The results must therefore be treated with caution. The FWHMs from the mean spectrum are plotted against the luminosity in the bottom panel of Fig. 7. There is no significant correlation between the variables. However, if we omit the data point for the narrow line Seyfert 1, NGC 4051, which clearly deviates from the other

points and highly influences the fit, we do obtain a marginally significant correlation. The correlation coefficient is  $-0.386$ , and its significance level is  $2.7 \times 10^{-2}$ . A linear fit gives

$$v_{FWHM}(\text{mean}) = (4108_{-65}^{+66}) \left( \frac{\lambda L_\lambda(5100\text{\AA})}{10^{44} \text{ergs s}^{-1}} \right)^{-0.271 \pm 0.012} \text{ km s}^{-1}. \quad (7)$$

FWHMs from the rms spectrum versus luminosity are plotted in the top panel of Fig. 7. The correlation coefficient is  $-0.540$  has a significance level of  $1.2 \times 10^{-3}$  and the best linear fit to the data is

$$v_{FWHM}(\text{rms}) = (3752_{-56}^{+57}) \left( \frac{\lambda L_\lambda(5100\text{\AA})}{10^{44} \text{ergs s}^{-1}} \right)^{-0.267 \pm 0.010} \text{ km s}^{-1}. \quad (8)$$

Thus, we find significant anticorrelations, in our incomplete sample, between the FWHM of the Balmer lines and the luminosity of the objects such that  $v_{FWHM} \propto L^{-0.27 \pm 0.01}$ . Our result indicates a stronger anticorrelation coefficient when  $v_{FWHM}(\text{rms})$  is used. While the above studies used only one epoch for each quasar in their measurements, our study uses the means of the luminosities and velocities for each object over 7.5 years, and averages both H $\alpha$  and H $\beta$ . The PG quasars'  $v_{FWHM}$  found in this study agrees with the ones found by Boroson & Green's (1992) to within  $\sim 10\%$ , except for two objects (PG 1351 and PG 1704) for which we measure significantly narrower lines. If we exclude those two objects, the anticorrelation

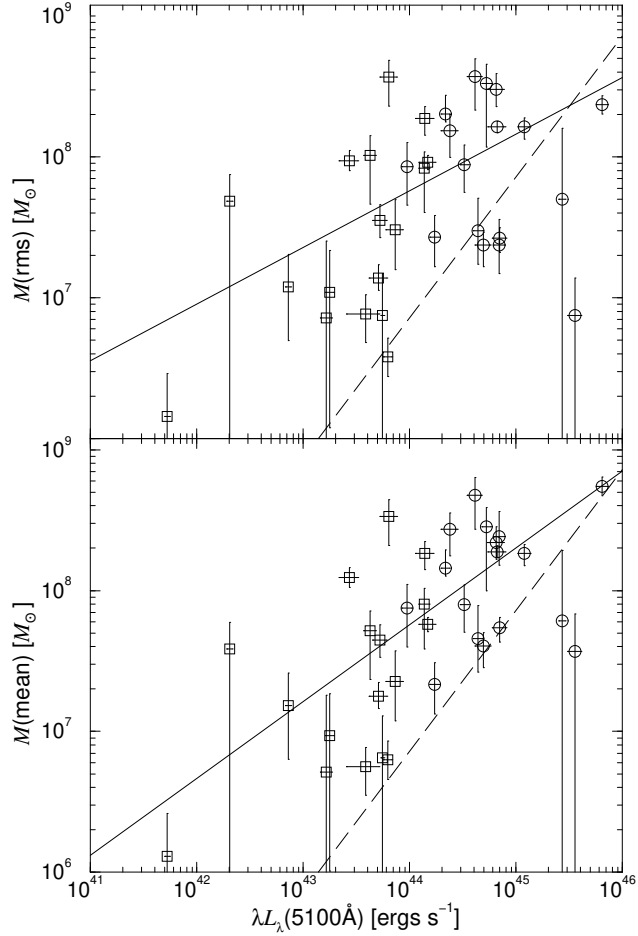


FIG. 8.— Mass—luminosity relations. Top: masses derived from  $v_{FWHM}$ (rms). Bottom: masses derived from  $v_{FWHM}$ (mean). Solid lines are the best fit to the data. Dashed lines are the Eddington limit based on a rough estimate for the bolometric luminosity (see text).

becomes weaker and its significance decreases. As the correlation we find is opposite to those found by previous studies, the issue of the velocity—luminosity relation needs further investigation, which is beyond the scope of this paper.

### 5.3. Mass—Luminosity Relation

Our two velocity estimates produce two mass estimates for each object (see Table 7 and § 4.3). Our mass estimates based on the determination of the FWHM from the mean spectra are plotted versus luminosity in the bottom panel of Fig. 8. The correlation coefficient between these two parameters is 0.646 and has a significance level of  $3.7 \times 10^{-5}$ . A linear fit gives

$$M(\text{mean}) = (5.71^{+0.46}_{-0.37}) \times 10^7 \left( \frac{\lambda L_\lambda(5100 \text{ \AA})}{10^{44} \text{ ergs s}^{-1}} \right)^{0.545 \pm 0.036} M_\odot \quad (9)$$

and is plotted as a solid line in the diagram.

The mass estimates based on the determination of the FWHM measured from the rms spectra are plotted in the top panel of Fig. 8. We find correlation coefficient of 0.473 with a significance level of  $4.7 \times 10^{-3}$ . A linear fit to this relation gives

$$M(\text{rms}) = (5.75^{+0.39}_{-0.36}) \times 10^7 \left( \frac{\lambda L_\lambda(5100 \text{ \AA})}{10^{44} \text{ ergs s}^{-1}} \right)^{0.402 \pm 0.034} M_\odot \quad (10)$$

and is also plotted as a solid line.

The results of the above two methods are not consistent. Moreover, while it is arguable that using the rms spectra to determine  $v$  is a better method (see § 4.3), the mass—luminosity correlation based on this measure is less significant. This can perhaps be attributed to the fact that the line fluxes in the rms spectra are weaker and hence the uncertainty in the corresponding FWHM larger.

Our M—L relation does not agree with the one found by Koratkar & Gaskell (1991b) of  $M \propto L^{0.91 \pm 0.25}$ , nor does it agree with the one found by Wandel et al. (1999) of  $M \propto L^{0.77 \pm 0.07}$ . However, when Wandel et al. (1999) use an unweighted linear fit they find a slope of 0.54 which is in good agreement with our result. We have used a linear regression analysis which takes into account the uncertainties in both coordinates (see § 4).

The fact that the scatter in the mass—luminosity relation is larger than that of the size—luminosity and velocity—luminosity relations may indicate that luminosity, rather than mass, is the variable that mainly determines the BLR size. In fact, from the individual size and velocity relations we expect:  $M \propto v^2 R_{BLR} \propto (L^{-0.27})^2 L^{0.7} = L^{0.16}$ , i.e., a weak dependence of mass on luminosity, with all AGN having similar masses. In practice, we have found a somewhat stronger dependence,  $M \propto L^{0.5 \pm 0.1}$ , but with a large scatter.

The M—L relation can be expressed in terms of the Eddington luminosity,  $L_{Edd}$ . Roughly estimating the bolometric luminos-

ity as  $L_{bol} \approx 9\lambda L_\lambda(5100\text{\AA})$ , we obtain an Eddington ratio of

$$\frac{L_{bol}}{L_{Edd}} \approx 0.13 \left( \frac{\lambda L_\lambda(5100\text{\AA})}{10^{44} \text{ ergs s}^{-1}} \right)^{0.5}. \quad (11)$$

The Eddington limit, based on this rough estimate for  $L_{bol}$ , is plotted as a dashed line in Fig. 8. Some of the quasars in our sample appear to be approximately at or beyond the Eddington limit. According to Fig. 8, the Eddington limit traces an envelope in the mass–luminosity plane (if we ignore the two lower right hand points, PG1700 and PG1704, which have very large errors). This depends, somewhat, on the factor chosen to estimate the bolometric correction, i.e. the rather uncertain slope of the unobserved UV continuum. However, if our chosen bolometric correction is realistic, we may be seeing a direct indication that AGN energy is generated by gas accretion.

Wandel (1999) reviews three classes of AGN mass estimation methods. While the X-ray variability method (using the shortest time scale for global luminosity variations as the light travel time across the Schwarzschild radius) and the accretion disk modeling method (deriving an accretion disk model that best fits the observed AGN continuum) suggest that the Eddington ratio increases with luminosity, Wandel (1999) notes that the kinematic methods (such as reverberation mapping) have yet to show a similar trend. Our reverberation mapping result (equation 11) indicates for the first time that the Eddington ratio increases with luminosity.

Models that suggest the bulk of the luminosity is due to energy release via mechanisms which radiate up to a set fraction of the Eddington luminosity are not consistent with the derived mass–luminosity relation. One such model is a geometrically thin, optically thick, accretion disk that requires  $L/L_{Edd} < 0.3$  to be self-consistent (Laor & Netzer 1989). Our finding suggests that the mass accretion rate grows with luminosity much faster than the central mass, which would mean very different disk properties in low- and high-luminosity sources. Our luminosity determination is based on the monochromatic flux at 5100 Å. In the thin disk model, this monochromatic flux may represent a different fraction of the object's bolometric luminosity in AGN of different masses. Thus, it is not clear that the thin accretion disk model can be ruled out by the new results.

## 6. SUMMARY

Spectrophotometric monitoring of a large, optically-selected quasar sample has shown clear correlations and well-defined time lags between the optical continuum and the Balmer-

line light curves. While the Seyfert 1 galaxies that have been studied in this manner all have optical luminosities  $< 1.5 \times 10^{44} \text{ ergs s}^{-1}$ , the new sample allows us to measure time lags in AGN with luminosities up to  $10^{46} \text{ ergs s}^{-1}$ . Our work increases the available luminosity range for studying the size–mass–luminosity relations in AGN by two orders of magnitude and doubles the number of objects suitable for these studies. We have combined our results for 17 quasars with data for 17 Seyfert 1 galaxies having reliable time lag measurements, and derived uniform estimates of BLR size, central masses, and luminosities for the combined sample.

Our main finding is that the BLR size scales with the 5100 Å luminosity as  $L^{0.70 \pm 0.03}$ . This is significantly different from Wandel et al.'s (1999) analysis and is also in contradiction with simple theoretical expectations, both suggesting  $R_{BLR} \propto L^{0.5}$ . We have also found that the velocity field of the BLR scales inversely with the luminosity,  $v_{FWHM} \propto L^{-0.27 \pm 0.01}$ . Combining the measured  $R_{BLR}$  with the observed FWHMs, we have obtained a mass–luminosity relation for AGN,  $M \propto L^{0.5 \pm 0.1}$ , which, however, has a large intrinsic scatter. The M–L correlations are based on two different estimates (mean and rms) of the FWHM of the Balmer lines and are not consistent with each other, despite the fact that the two measured values for the FWHM are generally consistent. Empirically, at least, it is not obvious which method of FWHM measurement is preferable.

Our results show the usefulness of long-term monitoring of high-luminosity AGN. There is a need to expand the luminosity range to include the highest luminosity quasars and this will require some 5–10 years of observations. Follow-up studies are also needed for some of the results obtained here, such as better determinations of the gas distribution in the BLR and the exact SED of the quasars. Future work using this sample will include the study of time-variable line profiles, lags between continuum bands, the intrinsic Baldwin relation, and more.

We are grateful to Brad Peterson for supplying us with the Seyfert 1 data and for many enlightening comments and discussions, and to the referee, Martin Gaskell, for his constructive advice. Ari Laor is acknowledged for very useful discussions. We thank John Dann and the WO staff for their expert assistance with the observations throughout the years. Research at the WO is supported by grants from the Israel Science Foundation. Monitoring of PG quasars at SO was supported by NASA grant NAG 5-1630. H.N. & S.K. acknowledge financial support by the the Jake Adler Chair of Extragalactic Astronomy. S.K. acknowledges financial support by the Colton Scholarships.

## REFERENCES

Alexander, T. 1997, in *Astronomical Time Series*, ed. D. Maoz, A. Sternberg, & E. M. Leibowitz (Dordrecht: Kluwer), 163

Bohlin, R. C., & Grillmair, C. J. 1988a, *ApJS*, 66, 209

Bohlin, R. C., & Grillmair, C. J. 1988b, *ApJS*, 68, 487

Boroson, T. A., & Green, R. F. 1992, *ApJS*, 80, 109

Collier, S. J. et al. 1998, *ApJ*, 500, 162

Dumont, A. -M., Collin-Souffrin, S., & Nazarova, L. 1998, *A&A*, 331, 11

Edelson, R. A., & Krolik, J. H. 1988, *ApJ*, 333, 646

Erkens, U., et al. 1995, *A&A*, 296, 90

Gaskell, C. M. 1988, *ApJ*, 325, 114

Gaskell, C. M. 1994, in *Reverberation Mapping of the Broad-Line Region in AGN*, ed. P. M. Gondhalekar, K. Horne, & B. M. Peterson (San Francisco: ASP), 111

Gaskell, C. M. 1996, *ApJ*, 464, L107

Gaskell, C. M., & Peterson, B. M. 1987, *ApJS*, 65, 1

Gaskell, C. M., & Sparke, L. S. 1986, *ApJ*, 305, 175

Gilbert, A. M., Eracleous, M., Filippenko, A. V., & Halpern, J. P. 1999, *AAS*, 194, 73.02

Giveon, U., Maoz, D., Kaspi, S., Netzer, H., & Smith, P. S. 1999, *MNRAS*, 306, 637 (Paper III)

Gondhalekar, P. M. 1990, *MNRAS*, 243, 443

Gondhalekar, D. M., et al. 1986, *MNRAS*, 222, 71

Jackson, N., et al. 1992, *A&A*, 262, 17

Joly, M., Collin-Souffrin, S., Masnou, J. L., & Nottale, L. 1985, *A&A* 152, 282

Kaspi, S. et al. 1996b, *ApJ*, 470, 336

Kaspi, S., Ibbetson, P. A., Mashal, E. & Brosch, N. 1995, *Wise Obs. Tech. Rep.*, No. 6

Kaspi, S., & Netzer, H. 1999, *ApJ*, 524, 71

Kaspi, S., Smith, P. S., Maoz, D., Netzer, H., Jannuzzi, B. T. 1996a, *ApJ*, 471, L75 (Paper II)

Koratkar, A. P., & Gaskell, C. M. 1991a, *ApJS*, 75, 719

Koratkar, A. P., & Gaskell, C. M. 1991b, *ApJ*, 370, L61

Koratkar, A. P., Pian, E., Urry, C. M., & Pesce, J. E. 1998, *ApJ*, 492, 173

Korista, K. T. 1991, *AJ*, 102, 41

Laor, A., & Netzer, H. 1989, *MNRAS*, 238, 897

Laor A., Fiore, F., Elvis, M., Wilkes, B. J., & McDowell, J. C. 1997, *ApJ*, 477, 93

Maoz, D., & Netzer, H. 1989, *MNRAS*, 236, 21

Maoz, D., Smith, P. S., Jannuzzi, B. T., Kaspi, S., Netzer, H. 1994, *ApJ*, 421, 34 (Paper I)

Maoz, D., Edelson, R. A., & Nandra, K. 2000, *AJ*, in press (astro-ph/9910023)

Nandra, K., Clavel, J., Edelson, R. A., George, I. M., Malkan, M. A., Mushotzky, R. F., Peterson, B. M., & Turner, T. J. 1998, 505, 594

Netzer, H. 1987, *MNRAS*, 255, 55

Netzer, H. et al. 1990, *ApJ*, 353, 108

Netzer, H. & Maoz, D. 1990, *ApJ*, 365, L5

Netzer, H. et al. 1996, *MNRAS*, 279, 429

Netzer, H., & Peterson, B. M. 1997, in *Astronomical Time Series*, eds., D. Maoz, A. Sternberg, and E. Leibowitz (Dordrecht: Kluwer), 85

O'Brien, P. T., & Gondhalekar, P. M. 1991, *MNRAS*, 250, 377

O'Brien, P. T., & Harries, T. J. 1991, *MNRAS*, 250, 133

O'Brien, P. T., Goad, M. R., & Gondhalekar, P. M. 1995, *MNRAS*, 275, 1125

Penston, V. M. 1991, in *Variability of Active Galactic Nuclei*, ed. H. R. Miller & P. J. Wiita (Cambridge, Cambridge Univ. Press), 343

Pérez, E., Penston, M. V., & Moles, M. 1989, *MNRAS*, 239, 55

Peterson, B. M. 1993, *PASP*, 105, 207

Peterson, B. M., & Wandel A. 1999, *ApJL*, 521, 95

Peterson, B. M., Pogge, R. W., Wanders, I., Smith, S. M., & Romanishin, W. 1995, *PASP*, 107, 579

Peterson, B. M., Wanders, I., Bertram, R., Hunley, J. F., Pogge, R. W., & Wagner, R. M. 1998a, *ApJ*, 501, 82

Peterson, B. M., Wanders, I., Horne, K., Collier, S., Alexander, T., Kaspi, S., & Maoz, D. 1998b, *PASP*, 110, 660

Peterson, B. M. et al. 1991, *ApJ*, 368, 119

Peterson, B. M. et al. 1999, *ApJ*, 510, 207

Press, W. H., Teukolsky, S. A., Vetterling, W. T., & Flannery, B. P. 1992, *Numerical Recipes*, Second Edition (Cambridge: University press), 660

Savage, B. D., & Mathis, J. S. 1979, *ARA&A*, 17, 73

Schmidt M., & Green, R. F. 1983, *ApJ*, 269, 352

Shields, J. C., Ferland, G. J., & Peterson, B. M. 1995, *ApJ*, 441, 507

Shuder, J. M. 1984, *ApJ*, 280, 491

Sitko, M. L. 1990, *ApJS*, 72, 777

Stirpe, G. M., Robinson, A., & Axon, D. J. 1999, in *Structure and Kinematics of Quasar Broad Line Regions*, ed. C. M. Gaskell et al. (San Francisco: ASP), 249

Ulrich, M. H., Courvoisier, T. J.-L., & Wamsteker, W. 1993, *ApJ*, 411, 125

Wandel, A. 1999, in *Structure and Kinematics of Quasar Broad Line Regions*, ed. C. M. Gaskell et al. (San Francisco: ASP), 213

Wandel, A., & Yahil, A. 1985, *ApJ*, 295, L1

Wandel, A., Peterson, B. M., & Malkan M. A. 1999, *ApJ*, in press (astro-ph/9905224)

White, R. J., & Peterson, B. M. 1994, *PASP*, 106, 879

Wisotzki, L., Wucknitz, O., Lopez, S., & Sorensen, A. N. 1998, *A&A*, 339, L73

Zheng, W. 1988, *ApJ*, 324, 801

Zheng, W., & Burbidge E. M., 1986 *ApJ*, 306, L67

Zheng W., Burbidge, E. M., Smith, H. E., Cohen, R. D., & Bradley, S. E. 1987, *ApJ*, 322, 164

Zheng W., Kriss, G. A., Telfer, R. C., Grimes, J. P., & Davidsen A. P. 1997, *ApJ*, 475, 469